

THE EXTREME OUTER REGIONS OF DISK GALAXIES: I. CHEMICAL ABUNDANCES OF HII REGIONS

Annette M. N. Ferguson^{1,2,3}

Department of Physics and Astronomy, The Johns Hopkins University, Baltimore, MD 21218

J. S. Gallagher²

Department of Astronomy, University of Wisconsin, Madison, WI 53706

Rosemary F. G. Wyse^{2,3}

Department of Physics and Astronomy, The Johns Hopkins University, Baltimore, MD 21218

ABSTRACT

We present the first results of an ongoing project to investigate the present-day chemical abundances of the extreme outer parts of galactic disks, as probed by the emission line spectra of a new sample of HII regions. The galaxies studied here, NGC 628, NGC 1058 and NGC 6946, are all late-type spiral galaxies, characterized by larger than average HI-to-optical sizes. Our deep H α images have revealed the existence of recent massive star formation, traced by HII regions, out to, and beyond, two optical radii in these galaxies (defined by the B-band 25th magnitude isophote). Optical spectra of these newly-discovered HII regions are used to investigate their densities, ionization parameters, extinctions and in particular their oxygen and nitrogen abundances. Our measurements reveal gas-phase abundances of O/H \sim 10-15% of the solar value, and N/O \sim 20-25% of the solar value, at radii of 1.5–2 R₂₅. Clear evidence also exists for diminished dust extinction ($A_V \sim 0$ –0.2) at large radii.

The combination of our measurements of outer disk HII region abundances with those for inner disk HII regions published in the literature is a powerful probe of the shape of abundance gradients over unprecedented radial baselines. The predictions of models of chemical evolution often diverge most strongly in the outer parts of galaxies. Both the oxygen and the nitrogen-to-oxygen abundances generally decrease with increasing radius. Within the limits of the current dataset, the radial abundance variations are consistent with single log-linear relationships, although the derived slopes can often differ considerably from those found if only inner disk HII regions are used to define the fit. The small number of HII regions in our present sample,

¹ Current Address: Institute of Astronomy, University of Cambridge, Madingley Road, Cambridge, UK CB3 0HA

²Visiting Astronomer, Kitt Peak National Observatory. KPNO is operated by AURA, Inc. under contract to the National Science Foundation.

³Visiting Astronomer, Lowell Observatory.

together with uncertainties in the calibrations of the empirical methods used here to determine abundances, limit the ability to constrain both subtle changes in the radial gradient and intrinsic scatter at a fixed radius. Nitrogen-to-oxygen ratios appear to be consistent with a combination of primary and secondary production of nitrogen. Interestingly, both the mean level of enrichment and the ratio of N/O measured in extreme outer galactic disks are similar to those values measured in some high redshift damped Lyman- α absorbers, suggesting that outer disks at the present epoch are relatively unevolved.

Subject headings: galaxies: abundances – galaxies: ISM – galaxies: spiral

1. Introduction

Radial variations in the abundances of elements within galaxies are well-established as providing important constraints on models of disk galaxy formation and evolution (eg. Pagel & Edmunds 1981; Vila-Costas & Edmunds 1992; Zaritsky, Kennicutt & Huchra 1994 (hereafter ZKH); Prantzos & Aubert 1995). HII regions play a unique role in such studies because they yield relatively reliable elemental abundances from measurements of emission line intensities. The early work of Searle (1971) and Shields (1974) used observations of HII regions in spirals to establish the existence of negative radial gradients in the abundance of oxygen. Subsequent work has shown that such gradients are a generic feature of disk galaxies, although the magnitude and the shape of the gradient, as well the characteristic abundance, are observed to vary considerably from galaxy to galaxy (eg. Vila-Costas & Edmunds 1992; ZKH).

Unfortunately, most HII region abundance studies carried out to date have probed only the bright, easily-observed inner regions of galactic disks, lying at or within the classical optical radius, R_{25} (defined by the B-band 25th magnitude isophote). It is well known, however, that disk galaxies have HI disks which extend to typically $\gtrsim 1.5\text{--}2 R_{25}$ (eg. Cayette et al 1994; Broeils 1994), and in some rare cases to $\gtrsim 3R_{25}$ (eg. van der Kruit & Shostak 1984). These outer regions are characterized by low HI columns, high gas fractions and long dynamical timescales and thus provide an opportunity to study star formation and chemical evolution in rather unique physical environments. Indeed, the outer regions of disks have physical properties which are reminiscent of those thought to exist during the early stages of galaxy formation, as well as those in giant low surface brightness galaxies, such as Malin 1 (eg. Pickering et al 1997). Studying the mean enrichment level, the shape of the abundance gradient and the amount of intrinsic scatter at fixed radius, in outer galactic disks will therefore forward our understanding of a broad range of astrophysical objects. Furthermore, since the predictions of models of chemical evolution often diverge most strongly in the outer parts of galaxies, abundance determinations extending as far in the outer disk as possible are needed to discriminate between competing theories.

Only a handful of outer disk HII regions have measured abundances and, of these, very few lie at galactocentric radii significantly beyond the optical radius (eg. Garnett & Shields 1987; Garnett et al 1992; Garnett & Kennicutt 1994). The bias of previous studies of HII regions to the inner disk has certainly been due in part to the lack of known HII regions lying at large radii. In the course of a large, deep, H α imaging survey to search for and study star formation in the extreme outer regions of disk galaxies (Ferguson 1997), we have discovered numerous faint HII regions in the low gas surface density ($N_{HI} \lesssim \text{few} \times 10^{20} \text{ cm}^{-2}$) outer limits of several galaxies. These HII regions are typically small (diameter $\sim 150\text{--}500$ pc) and of low luminosity ($L_{H\alpha} \sim 1\text{--}10 L_{Orion}$), and do not clump into the giant complexes which populate the inner disks of spiral galaxies. They are often observed to trace out narrow spiral arms, which are sometimes coincident with underlying HI arms and faint stellar arms ($\mu_B \sim 26\text{--}28 \text{ mag}/\square''$). A study of the ongoing and past star formation in the outer disks of these galaxies and its implications for models of disk galaxy evolution will be presented elsewhere (Ferguson et al, 1998a,b).

We present here the first results from a long-slit spectroscopic study to determine the chemical abundances in the extreme outer parts of nearby disk galaxies, using the emission line spectra of our newly discovered HII regions. This paper presents results for three late-type spiral galaxies, namely NGC 628, NGC 1058 and NGC 6946. These galaxies have particularly extended disks of neutral hydrogen and are amongst our best examples of galaxies with extreme outer disk star formation. A summary of their properties is presented in Table 1. Chemical abundances for HII regions in the inner disks of NGC 628 and NGC 6946 have been derived by McCall, Rybski & Shields (1985: hereafter MRS). Chemical abundances have not been previously measured for HII regions in NGC 1058, and we present here a study of both inner and outer disk HII regions in that galaxy.

2. Observations

The typical H α fluxes of the outer HII regions we have identified range from $1\text{--}70 \times 10^{-15} \text{ erg s}^{-1} \text{ cm}^{-2}$, which for reference is roughly 10–1000 times fainter than the usual HII regions in late type spirals which have previously been studied spectroscopically (eg. MRS, ZKH). Our strategy was to first target the brightest outer disk HII regions in our sample. The data discussed here were obtained during November 1994, using the KPNO 4m telescope and the RC-spectrograph + T2KB. The T2KB chip was run with a gain of $2e^-/\text{ADU}$ and readnoise of $\sim 4e^-$. We used a $2'' \times 300''$ slit with a single moderate-resolution grating (KPC10-A; 316 l/mm) to cover the wavelength range of range 3600–7500Å, with spectral resolution of $\sim 7\text{Å}$.⁴ The

⁴During a previous observing run, the data from which will be reported in a future paper, we used higher spectral resolution, requiring two gratings, in an attempt to detect the temperature-sensitive [OIII] $\lambda 4363$ line. Such resolution was required in order to separate the [OIII] $\lambda 4363$ line from any scattered HgI $\lambda 4358$ emission. Unfortunately, we failed to detect [OIII] $\lambda 4363$ at all and so switched strategies to a simpler observing mode.

grating was used in first order with an order-blocking filter (WG345) to eliminate second-order blue light from below $\sim 3200\text{\AA}$. The seeing was typically $1.5\text{--}2''$. Of the three nights of our run, two nights were mostly clear, hampered only by light to moderate cirrus during the latter parts of each night, but the third night was completely lost. In this paper, we discuss only a subset of the data obtained during the November run, consisting of measurements of HII regions in the disks of NGC 628, NGC 1058 and NGC 6946.

Blind offsets were required for all of our target outer HII regions. These were derived from deep narrow-band images obtained using the KPNO 0.9m and Lowell 1.8m telescopes, and were based on either nearby bright stars or the nucleus of the galaxy. The images were astrometrically calibrated using a grid of stars measured on the digitised POSS plates and are accurate to $\lesssim 0.5''$. Individual exposure times were 30 min per region and we usually obtained 2–4 exposures per target region, depending on the faintness of the target. Experience indicated that if no metal lines were detected in a single 30 min exposure, then there was negligible chance of obtaining useful data for abundance determinations by stacking additional exposures. Most objects were observed at low airmass and we rotated the slit to parallactic angle whenever possible to eliminate the loss of blue light. We also attempted to position the slit in such a manner as to include as many HII regions as possible, but the small angular size, faintness and relative isolation of our outermost targets made this difficult. Spectra of He-Ne-Ar lamps were obtained before and after each object exposure, and we made multiple observations of standard stars from the list of Massey et al (1988).

In Figures 1–3, we show continuum-subtracted $H\alpha$ images of each galaxy with the target HII regions identified. Table 2 lists the identifications, positions and properties of our sample of HII regions. The diameters and fluxes presented are approximate and are intended simply to illustrate the range in physical properties which exists within our sample. In particular, it is very difficult (and subjective) to assign sizes and fluxes to inner disk HII regions, which often are part of large complexes composed of many ‘cores’. We have not corrected the fluxes and luminosities for the effects of internal extinction. Most of the outer disk HII regions in our sample have luminosities consistent with their being ionized by only a few equivalent O5V stars, as calculated using the Lyman continuum fluxes in Vacca et al (1996); these estimates are strictly lower limits to the number of enclosed massive stars as the HII regions may well not be ionization bounded (eg. see the discussion of the origins of diffuse ionized gas by Ferguson et al 1996a,b). Two inner disk HII regions from the sample of MRS are included in our sample in order to provide an external consistency check on our measurements.

see ferguson.fig1.jpg

Fig. 1.— An $H\alpha$ continuum-subtracted image of NGC 628 obtained using the KPNO 0.9m, with the target HII regions identified. R_{25} is marked. North is to the top and east to the left.

see ferguson.fig2.jpg

Fig. 2.— A mosaiced $H\alpha$ continuum-subtracted image of NGC 1058 obtained using the Lowell 1.8m, with the target HII regions identified. R_{25} is marked. North is to the top and east to the left.

see ferguson.fig3.jpg

Fig. 3.— An $H\alpha$ continuum-subtracted image of NGC 6946 obtained using the KPNO 0.9m, with the target HII regions identified. R_{25} is marked. North is to the top and east to the left.

3. Data Analysis

Preliminary data reduction was carried out using standard procedures. A DC offset was subtracted from each frame using the overscan region. Bias frames and quartz lamp exposures were used to remove any residual structure in the DC offset and pixel-to-pixel gain variations respectively. Dark frames were also obtained but the dark current was found to be negligible and the frames were not utilized in the analysis. Exposures of the twilight sky were obtained to map out the illumination pattern along the slit, and flatten the data in the spatial direction.

One dimensional spectra were extracted with apertures ranging in size from 3–15'', depending on the seeing, and on the size and brightness of the object in question. The sky to be subtracted was selected from adjacent regions, and fit with a low order polynomial. An important step in the extraction process is mapping the location of the spectrum at each point along the dispersion axis. In the brightest HII regions observed, this ‘trace’ could be well-defined, and revealed only a small amount of distortion from the blue to the red, which was typically much less than the size of the extraction box. Only a weak continuum, if any, was present in the outer disk HII regions however. In those cases where we could not trace the continuum along the entire dispersion axis, we chose to fit a low order polynomial anchored to the position of one of the brightest lines present. The individual extracted spectra were wavelength calibrated using He-Ne-Ar exposures, with the typical accuracy of the transformation being a few tenths of a pixel, or equivalently $\sim 0.5 \text{ \AA}$. Flux calibration was carried out using observations of standard stars (with the same slit width as our program objects), and the sensitivity functions showed residuals of only $\sim 0.02\text{--}0.03$ magnitudes (after a zeropoint offset). At this point, individual spectra of the same HII region were checked for consistency and then averaged together. Spectra that had been dispersion corrected, but not flux calibrated, were also averaged for the purpose of computing uncertainties in the line intensities. In Figure 4, we present extracted, combined, calibrated spectra for 4 HII regions in NGC 1058, which are representative of the typical spectra obtained in this study.

Inspection of the spectra reveals the presence of many emission lines. Most prominent are the bright oxygen, nitrogen and sulfur lines, as well as the Balmer lines of hydrogen. In addition, several HII region spectra show detections of fainter lines, such as those due to helium, argon, neon and in some cases neutral oxygen. We focus here on only those bright lines which lead to determinations of the oxygen and nitrogen abundances through the semi-empirical methods discussed below in section 4.2. Emission line fluxes were measured via gaussian fits to the line profiles. The logarithmic extinction at $H\beta$, $C(H\beta)$, was derived from measurements of the Balmer lines, using the equation

$$\frac{I_\lambda}{I_{H\beta}} = \frac{F_\lambda}{F_{H\beta}} 10^{C(H\beta)f(\lambda)}$$

where I_λ is the intrinsic line flux, F_λ is the observed line flux, and $f(\lambda)$ is the Galactic reddening function normalized to $H\beta$. The reddening function of Seaton (1979), was adopted, as parametrized by Howarth (1983), and assuming $R=A_V/E(B-V)=3.1$. Intrinsic Balmer line ratios were taken from Osterbrock (1989), assuming an electron density of $N_e=100 \text{ cm}^{-3}$ and an electron

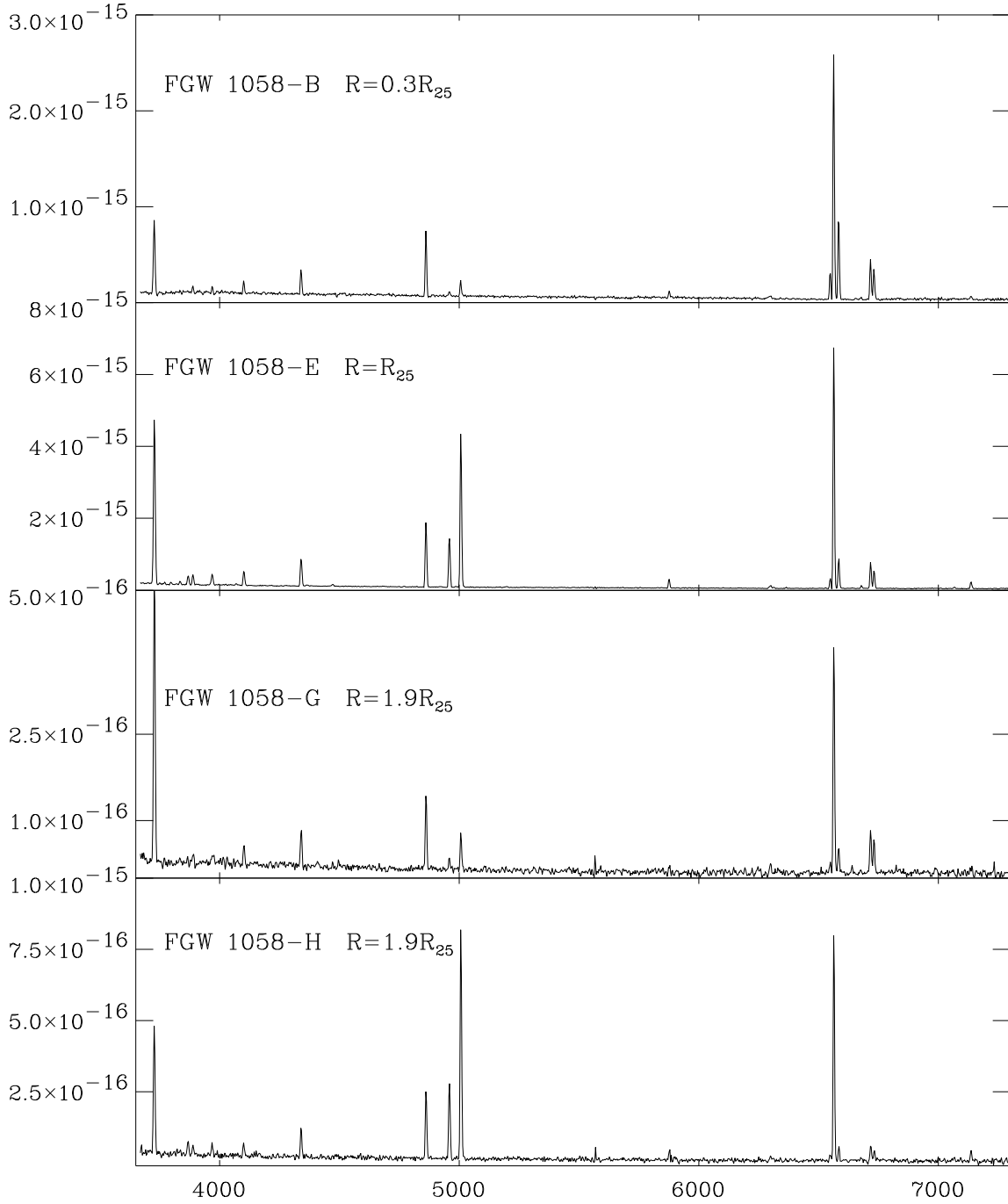


Fig. 4.— Representative spectra from this study. Shown are four of the HII regions observed in NGC 1058, displayed in order of increasing galactocentric radius (and metal abundance). The last two spectra represent HII regions at the same radius, which exhibit different excitations. The units are $\text{erg s}^{-1} \text{cm}^{-2} \text{Å}^{-1}$.

temperature $T_e=10^4$ K. The determination of the amount of underlying stellar Balmer absorption is an important concern in the estimation of the required extinction correction. Our data are of insufficient S/N to determine the absorption equivalent width directly, so we adopted the standard approach of assuming a correction of 2\AA to the measured equivalent width due to underlying stellar absorption (eg. MRS; Oey & Kennicutt 1993), and we proceeded to derive the logarithmic extinction at $H\beta$ based on the $H\beta$ and $H\alpha$ lines alone. We also corrected the forbidden-line/ $H\beta$ ratios for the effects of underlying $H\beta$ absorption, but this is generally a small effect since most spectra have moderate to large $H\beta$ equivalent widths.

Formal errors in the derived line ratios were determined by summing in quadrature the statistical noise from the number of counts, the uncertainty in the continuum placement (proportional to the width of the line times the RMS in the nearby continuum, corrected for the effects of pixelization), and the uncertainty in the flux calibration. In addition, the error in the $C(H\beta)$ term was accounted for when deriving extinction-corrected line ratios. Tables 3–5 present the observed line intensities, both uncorrected and corrected for reddening and Balmer absorption, as well as some relevant line-ratios for our sample of HII regions. Formal errors on the quantities are indicated in parentheses.

4. Deriving Nebular Abundances

4.1. The Direct Method

The ‘direct’ method for determining chemical compositions from nebular emission lines requires a knowledge of the electron temperature (and density) of the emitting gas in order to transform reddening-corrected emission line ratios to ionic abundance ratios, and finally to elemental abundances (eg. Osterbrock 1989). The electron temperature T_e is commonly derived from the O^{++} ion, via the ratio

$$\frac{[\text{OIII}] \lambda 4959 + [\text{OIII}] \lambda 5007}{[\text{OIII}] \lambda 4363} = \frac{7.73 \exp^{(3.29 \times 10^4)/T}}{1 + 4.5 \cdot 10^{-4} (N_e/T^{1/2})}$$

(Osterbrock 1989). Unfortunately, the temperature sensitive $[\text{OIII}] \lambda 4363$ line is typically very weak in extragalactic HII regions, and decreases in strength rapidly with increasing abundance; as a result, this method is limited to only the hottest (ie. most metal poor) and brightest objects. The faintness of our outer disk HII regions, coupled with the low resolution of our spectroscopy, severely limits the detectability of this key diagnostic line. A marginal detection of $[\text{OIII}] \lambda 4363$ was made in one of the individual spectra we obtained for the brightest outer disk HII region of our sample, 1058–E, but the significance of the detection is low. It can be used only to place an upper limit on the electron temperature of the region, and hence a lower limit on the oxygen abundance. We measure $[\text{OIII}] \lambda 4363/H\gamma \lesssim 0.067$, which, when combined with measurements of the $[\text{OIII}] \lambda \lambda 4959, 5007$ lines, translates into an upper limit of 12,700K on the temperature in the O^{++} zone (assuming $N_e = 100 \text{ cm}^{-3}$), and a lower limit on the oxygen abundance of

$\log(\text{O}/\text{H}) \gtrsim -4.07$ (both derived using the FIVEL program (de Robertis, Dufour & Hunt 1987) as implemented in IRAF). As will be shown below, this limit is consistent with the abundance derived via the semi-empirical method.

4.2. Semi-Empirical Methods

Fortunately, in the absence of a reliable [OIII] $\lambda 4363$ detection, there exist alternative methods for deriving nebular abundances which rely on observations of the bright lines alone (eg. Pagel et al 1979, Skillman 1989, McGaugh 1991, Thurston et al 1996). Empirical methods to derive the oxygen abundance exploit the inter-relationship between O/H, T_e and the intensities of the strong lines, [OII] $\lambda 3727$ and [OIII] $\lambda\lambda 4959, 5007$, via the parameter

$$R_{23} = \frac{[\text{OII}] \lambda 3727 + [\text{OIII}] \lambda\lambda 4959, 5007}{\text{H}\beta}.$$

As O/H decreases, the cooling efficiency of the nebular gas drops because there are fewer metal ions, and as a result T_e increases. This leads to a substantial brightening in the 4959Å and 5007Å lines, and hence an increase in R_{23} . On the other hand, as O/H increases, cooling becomes more efficient leading to a decrease in T_e . Most of the cooling then occurs through the fine-structure IR lines at 52 μm and 88 μm , leading to a decrease in the strength of the optical [OIII] lines and therefore in R_{23} . These variations in [OIII] line strength can clearly be seen in the representative spectra shown in Figure 4, which are stacked in order of decreasing metallicity. This simple relationship between R_{23} and O/H gets complicated by the fact that at very low O/H ($\sim 30\%$ solar⁵), the sheer lack of oxygen causes the bright lines (and hence R_{23}) to decrease as O/H decreases, due to the growing importance of Ly α cooling (Edmunds & Pagel 1984). As a result, while a single value of R_{23} can uniquely specify O/H over most of the range in metallicity, there is a turnover region (20–50% solar) where the relationship becomes double valued.

There have been several calibrations of the O/H– R_{23} relationship over the past years, based on both observations of HII regions with known abundances and the results of photoionization models (eg. Edmunds & Pagel 1984, MRS, Dopita & Evans 1986, Skillman 1989, McGaugh 1991, ZKH). Of particular importance for the present study is the calibration at the low abundance end ($\log(\text{O}/\text{H}) < -3.8$), and in the turnover region ($-3.4 \gtrsim \log(\text{O}/\text{H}) \gtrsim -3.8$) where a single value of R_{23} corresponds to two values of O/H. Skillman (1989) and McGaugh (1991) have illustrated the importance of accounting for the ionization state of the nebula in deriving an abundance estimate at low metallicities, however only the McGaugh calibration takes explicit account of this (see McGaugh 1994). McGaugh’s calibration has the further advantages that with it one can predict oxygen abundances on both upper and lower branches of the O/H– R_{23} relation, and also the

⁵We adopt $\log(\text{O}/\text{H})_{\odot} = -3.07$ and $\log(\text{N}/\text{O})_{\odot} = -0.88$ from Anders & Grevesse (1989).

volume averaged ionization parameter U , defined as

$$U = \frac{Q}{4\pi R_s^2 N c}$$

where Q is the ionizing photon luminosity, R_s is the radius of the Strömgen sphere, N is the number density of the gas and c the speed of light. For these reasons, we have adopted this calibration here.

Several methods have been proposed by which to distinguish between upper and lower branches for objects with values of R_{23} which place them in the double-valued region. McGaugh (1994) advocates the use of the $[\text{NII}] \lambda 6584 / [\text{OII}] \lambda 3727$ ratio, noting that it varies monotonically with O/H and that it is not very sensitive to the ionization parameter U since the two ions have similar ionization potentials. The division between upper and lower branches of R_{23} is fairly well-defined, with $\log([\text{NII}]/[\text{OII}]) > -1$ (reddening-corrected) indicating the upper branch and $\log([\text{NII}]/[\text{OII}]) < -1$ indicating the lower branch. Another diagnostic which has been used in the literature is the value of the line ratio $[\text{OIII}]/[\text{NII}]$ (eg. Skillman 1989), with the transition between upper and lower branches occurring at $\log([\text{OIII}]/[\text{NII}]) \sim 2$. While this parameter also varies monotonically with abundance, it is sensitive to the ionization parameter and is thus of limited use in the low abundance regime where such effects are important.

In Figure 5, we plot our HII regions on the model grid of $\log(O/H) - \log R_{23}$ from McGaugh (1991). One can clearly see the effect of the ionization parameter, U , in the turnover region and on the lower branch. All models converge towards a single upper branch, reflecting the fact that R_{23} is insensitive to U in this regime. As can be seen, our outer disk HII regions cluster around the ‘knee’ of the calibration. We have also overplotted a heterogeneous sample of HII regions which have oxygen abundances determined in the literature via the ‘direct’ method (see Section 5.2 for a discussion of this sample). The objects in this sample populate the same general region of the diagram as the HII regions in our sample. As will be discussed in detail below, comparison of the abundances determined via the ‘direct’ method and via the model calibration for this sample show very good agreement. Thus, the McGaugh calibration generally provides reliable abundance estimates for objects which lie in this region of the diagram.

Nitrogen to oxygen abundances (N/O) may be determined in the absence of a measurement of the strength of $[\text{OIII}] \lambda 4363$ by the algorithm recently proposed by Thurston et al (1996), again requiring only observations of the bright lines $[\text{NII}]$, $[\text{OII}]$ and $[\text{OIII}]$. The relationship, which is based on the same premise as that of the relationship between oxygen abundance and R_{23} , is calibrated by the results of photoionization modelling. This calibration does not take account of the fact that, for oxygen abundances lower than $\sim 25\%$ solar, a non-unique relation exists between O/H and R_{23} .

In Table 6, we list the derived oxygen and nitrogen-to-oxygen abundances for our sample, as well as the mean volume averaged ionization parameter, derived by our adopted techniques.

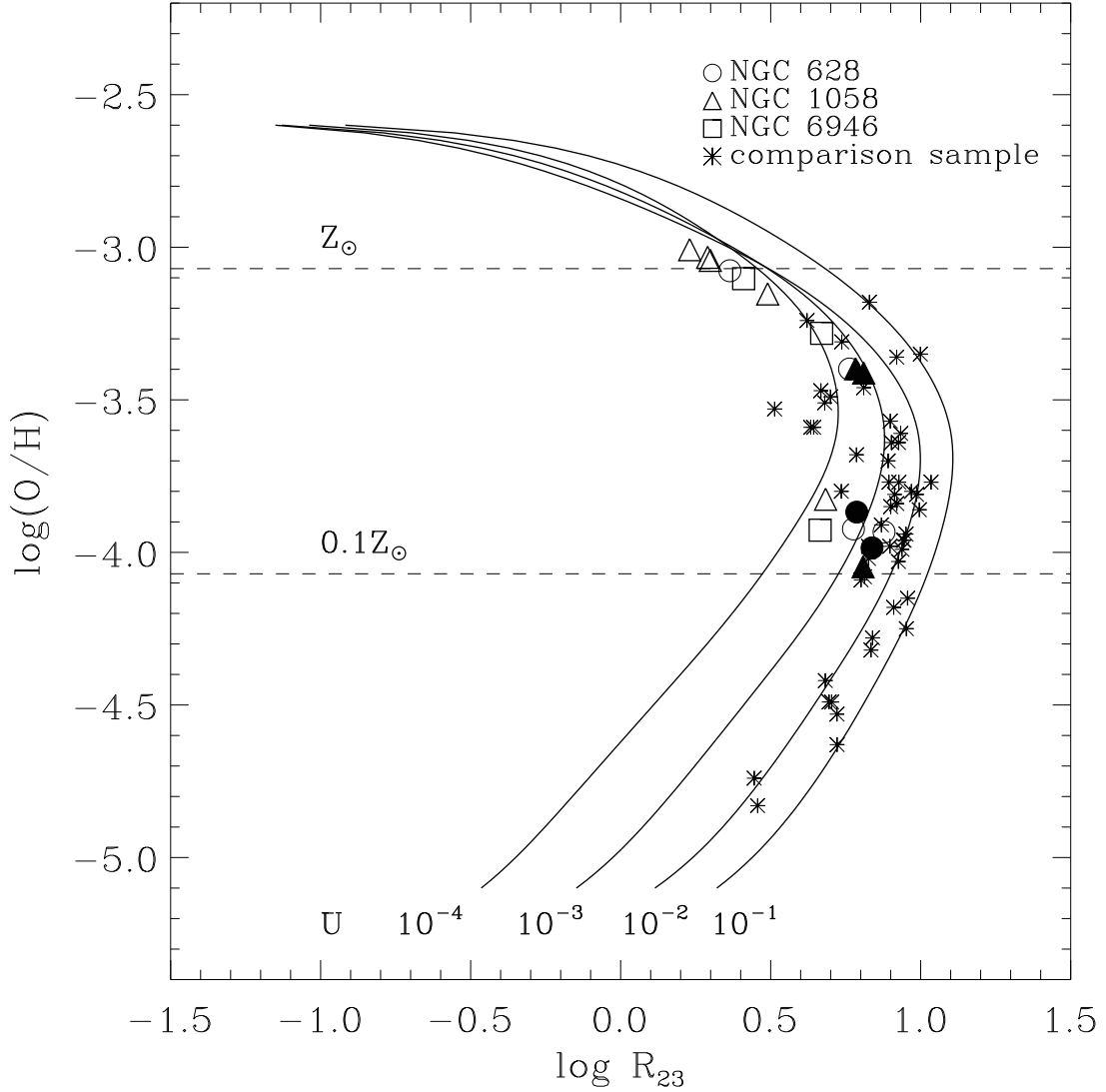


Fig. 5.— Model grid in the $\log(O/H)$ – $\log(R_{23})$ plane from McGaugh (1991). These models have been calculated for an upper mass cutoff of $60 M_{\odot}$. One can see the important effect of the ionization parameter, U , at low abundances. Overplotted on the grid are our sample of HII regions, as well as a heterogeneous sample of objects amassed from the literature (see text). Our HII regions occupy the same region of the diagram as this comparison sample, for which the McGaugh calibration is shown to reliably predict abundances (see Section 5.2).

5. Uncertainties

The uncertainties in the derived metallicities are a combination of both measurement errors and the intrinsic uncertainties in the model calibrations. As we will show below, various tests reveal that the formal errors on the line strengths appear to underestimate considerably the actual uncertainties in the line ratios, and in the final derived chemical abundances, and thus are of limited use for understanding the intrinsic uncertainty in our abundance estimates.

5.1. Measurement Errors

Measurement errors can arise from a variety of causes, such as extraction, sky subtraction, varying sky conditions and profile-fitting. We investigated the magnitude of the measurement errors in our data by conducting a series of experiments. First of all, we compared the line intensity measurements as derived from two different techniques – gaussian fitting and direct integration under the line profile. Defining the ‘mean fractional difference’ to be the result from either method minus the mean, divided by the mean, we find values of $1\% \pm 3\%$. While the mean fractional difference was greatest at the smallest fluxes, it is still less than 10%. Next, we compared line strength measurements for those HII regions for which we had obtained multiple spectra (that were subsequently combined). Since multiple observations of a given HII region were always made consecutively, this comparison should not be influenced to a great extent by slit-positioning. Considering only those lines which are well-detected, we calculate the mean fractional difference from multiple line measurements to be $8\% \pm 10\%$. Fainter lines tend to show more scatter than strong lines, for example [OIII] $\lambda 4959$ and [NII] $\lambda 6548$ have mean fractional differences of $\sim 15\%$. A conservative estimate of the uncertainties in the individual line strengths inferred from this comparison is $\pm 10\%$, from which we expect uncertainties of $\sim 15\%$ in the line ratios.

We also calculated the mean values of the ratios [OIII] $\lambda 5007$ /[OIII] $\lambda 4959$ and [NII] $\lambda 6854$ /[NII] $\lambda 6548$ for the HII regions in our sample. Since these ratios have a fixed theoretical value, comparison of our sample average with the expected values provides an additional gauge of our measurement errors. Considering again only those lines which are well-detected, we find $\langle [\text{OIII}] \lambda 5007 / [\text{OIII}] \lambda 4959 \rangle = 2.88$ with standard deviation 0.31 and $\langle [\text{NII}] \lambda 6854 / [\text{NII}] \lambda 6548 \rangle = 2.96 \pm 0.39$, which compare favourably to the theoretical values of 2.88 (Nussbaumer & Storey 1981) and 2.95 (Mendoza & Zeppen 1982) respectively.

As a final check on measurement errors, we included in our sample two HII regions which were observed by MRS. Despite the likely differences in pointings and aperture sizes employed, we find an excellent agreement in the values of R_{23} ; $\Delta \log(R_{23}) = 0.144$ for FGW 628–A (MRS identification N0628(-074,-022)) and -0.068 for FGW 6946–A (MRS identification N6946(+182,+103)). These differences in R_{23} lead to differences of only -0.08 and 0.07 dex in $\log(\text{O}/\text{H})$, and -0.16 and 0.08 in $\log(\text{N}/\text{O})$.

In summary, these various tests reveal that our measurement errors are small, and we conservatively estimate line ratios to be accurate to better than 15%, or ~ 0.1 dex.

5.2. Calibration Errors

The dominant source of uncertainty in our results is without a doubt that due to the model calibrations of the semi-empirical relationships between line strength and elemental abundance. Propagating the formal errors on the line strengths through the equations used to derive the abundances produces formal errors on the metallicities of only ~ 0.05 dex. As we will discuss below, the uncertainty in the absolute value of the calibration is likely to be much larger than this.

Uncertainties in the calibration arise from the limitations in the inputs to the models used to construct the calibration, and from the ability of the calibration to reproduce model input data, and indeed to reproduce the values of chemical abundances which have been determined via a measurement of the electron temperature. As discussed by McGaugh (1994), while these uncertainties can have an important effect on the absolute metallicities derived, they have a much smaller impact on the relative values.

One of the most important input parameters is the shape of the ionizing spectrum, which depends on both the mass and the metallicity of the ionizing stars (McGaugh 1991). McGaugh (1991) treats this problem by assuming a cluster containing several tens of OB stars is responsible for the ionization, which when averaged over, produces a constant ionizing spectrum, relatively insensitive to both the metallicities and individual effective temperatures of the enclosed stars, and hence the IMF. We note however that many of our outer disk HII regions, if ionization-bounded, are consistent with ionization by only a few massive stars (see Table 2) and hence the assumptions which have gone into McGaugh’s calibration may not be entirely appropriate for the objects under study here.

Concerning the ability of the calibrations to reproduce model input data, both McGaugh(1994) and Thurston et al (1996) report relative uncertainties of 0.1–0.2 dex over a wide range in metallicities. In the turnover region where R_{23} is double-valued, McGaugh (1994) estimates uncertainties of $\gtrsim 0.2$ dex, although as he points out they cannot be too much larger than this since strong R_{23} guarantees that an HII region lies in the range $-3.4 \geq \log(\text{O}/\text{H}) \geq -3.8$. Thurston et al (1996) see increasing deviations from the output, relative to model input, at low metallicities, but their conclusion is based on tests with only two low metallicity models: at 30% solar the deviation is < 0.1 dex whereas it is ~ 0.3 dex for the lowest metallicity model tested, which has an oxygen abundance of 7% solar.

Perhaps the most robust measure of the accuracy of the semi-empirical technique is a direct comparison of predicted abundances with those measured for low metallicity HII regions which have published abundance determinations based on a measurement of the electron temperature. We have gathered from the literature a sample of low metallicity HII regions, in a heterogeneous

set of parent galaxies, ranging from low metallicity dwarfs, including blue compact dwarfs (eg. Izotov et al 1994, Skillman & Kennicutt 1993, Skillman et al 1994, Miller 1994), irregulars (Webster & Smith 1983, Pagel et al 1980, Miller 1994) and spirals (Webster & Smith 1983, Edmunds & Pagel 1984, Pagel et al 1979, 1980, Garnett et al 1997a, Vilchez et al 1988). The sample also includes two outlying HII regions in the spirals M81 and M101 (Garnett & Shields 1987, Garnett & Kennicutt 1994); the M81 HII region is comparable in luminosity to those outer disk HII regions in our sample, having an H α luminosity of 4×10^{37} erg s $^{-1}$, while the M101 HII region is significantly more luminous.

The top panel of Figure 6 shows the difference between the ‘direct’ abundance determination (using the derived value of T_e) and that which is returned by the McGaugh calibration based on only the bright line strengths. As can be seen, the agreement between the two techniques improves significantly with decreasing abundance. While the larger discrepancy between the two techniques at high abundances may be due in part to shortcomings of the McGaugh calibration (for example, the lack of account for dust and depletion of heavy elements (see Shields & Kennicutt 1995)), it also reflects the increasing difficulty to measure accurate [OIII] λ 4363 strengths, and hence abundances via the ‘direct’ method, at metallicities close to solar⁶. We confirm the effect noted by McGaugh (1991) that the model calibration tends to slightly overpredict O/H at very low abundances. Still, the agreement between the independent determinations is generally very good, with an average offset of only -0.02 dex, and a standard deviation of 0.28 dex across the entire range of abundances spanned by our comparison sample. Over the particular region of interest for outer disk HII regions (10–30% solar), we find a mean offset between the different methods of -0.06 ± 0.23 dex. Hence, we will adopt 0.2 dex as the typical uncertainty in our derived oxygen abundances.

The bottom panel of Figure 6 shows the same comparison for the nitrogen-to-oxygen abundances determined via the Thurston et al (1996) calibration. As can be seen, the Thurston calibration provides N/O abundances which are in excellent agreement with those measured directly, deviating significantly only at extremely low metallicities. Averaging over all metallicities, we find a mean offset of 0.06 dex with a standard deviation of 0.16 dex. Over our prime region of interest (10–30% solar), the mean offset between the ‘direct’ abundance and model predictions is only -0.03 dex and the dispersion 0.08 dex. We also confirm their noted trend of the model under-predicting true abundances at very low O/H; systematic deviations of $\gtrsim 0.3$ dex appear for metallicities less than 5% solar. Thus, the semi-empirical techniques adopted in the present work appear to be able to reproduce (surprisingly) well the chemical abundances in this heterogeneous sample of low metallicity objects. In the discussion that follows, we will thus adopt a ± 0.2 dex uncertainty in our oxygen abundances and ± 0.1 dex in nitrogen-to-oxygen abundances.

⁶For those HII regions which clearly lie on the upper branch, we also calculated what the abundance would be if we used the R₂₃ calibration of ZKH. We find an average offset of 0.13 ± 0.06 dex between the different determinations of log(O/H), which is consistent with the uncertainty produced by either method alone.

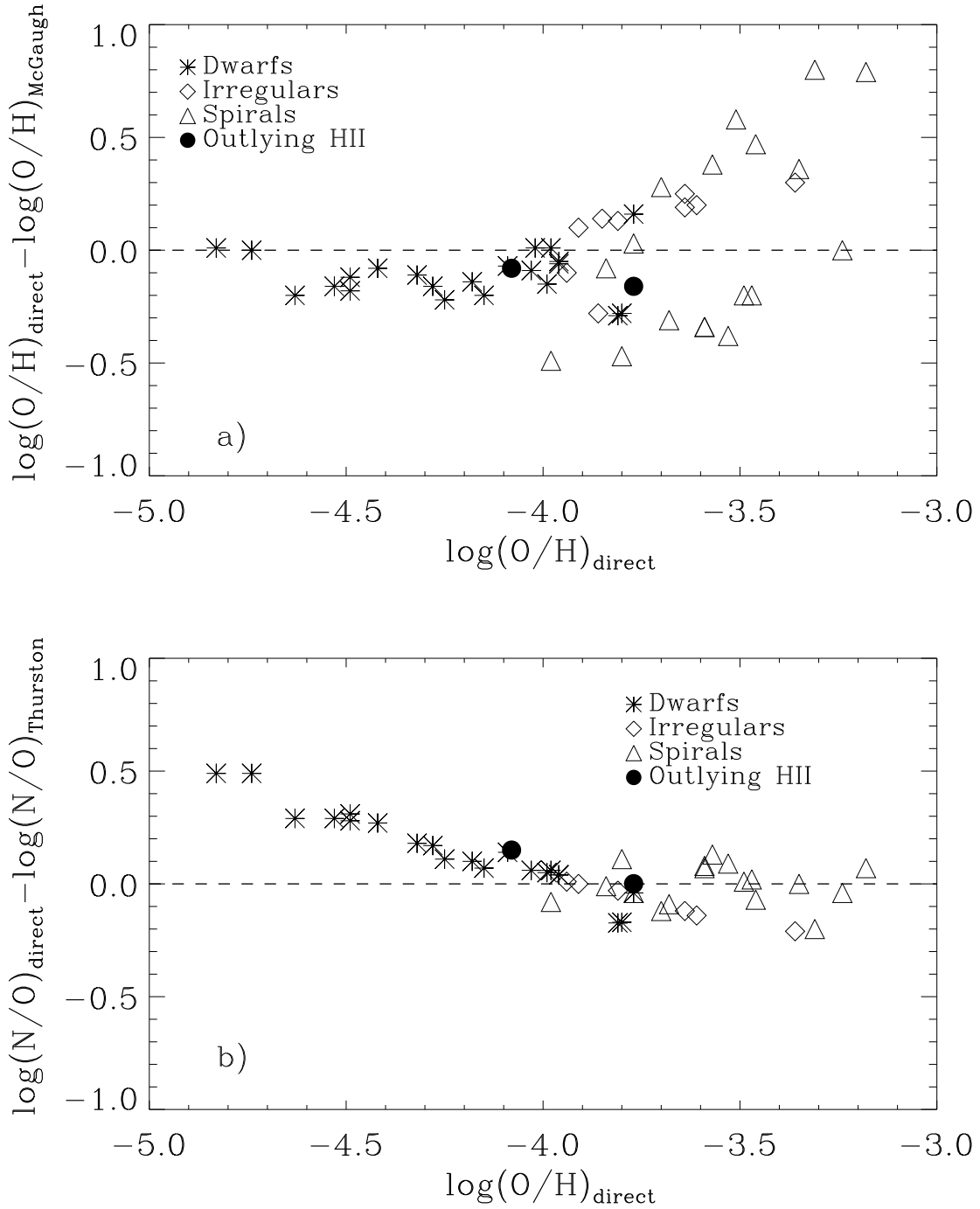


Fig. 6.— Comparison of O/H (a) and N/O (b) abundances determined from the ‘direct’ and semi-empirical techniques, expressed as a function of oxygen abundance. The data points represent a heterogeneous sample of low metallicity objects as described in the text. Over the prime region of interest for outer disk HII regions (10-30% solar), we find very good agreement between empirically-determined abundances and those determined from a measure of the electron temperature.

6. Results

6.1. Electron Densities

Electron densities can be estimated via the ratio of the [SII] $\lambda\lambda 6717, 6731$ lines (eg. Osterbrock 1989). The derived ratios for our entire sample are plotted in Figure 7 as a function of deprojected radius, normalised to the optical radius. The horizontal line indicates the low density limit of 1.42 (Czyzak et al 1986); HII regions with ratios comparable to this value are not affected by collisional de-excitation while those with lower values are. As can be seen, most of our sample appears consistent with the low density limit and hence we infer electron densities $\lesssim 100 \text{ cm}^{-3}$. There is one notable exception, FGW 1058–C, for which we infer a density of $\sim 10^3 \text{ cm}^{-3}$. No evidence exists for trends in electron density with galactocentric radius.

6.2. Ionization Parameter

The ionization parameter of a nebula, previously defined in Section 4.2, is essentially the local ratio of Lyman–continuum photons to gas density, which determines the degree of ionization at any particular location within the nebula. Figure 8 shows the variation of the mean volume averaged ionization parameter, $\langle U \rangle$, as derived by the McGaugh (1994) calibration, as a function of both galactocentric radius and oxygen abundance. HII regions at large radii are observed to exhibit a large range in $\langle U \rangle$, and there is no obvious trend in ionization parameter with either radius or oxygen abundance. This latter finding is in agreement with the results of ZKH and Kennicutt & Garnett (1996), but contrary to Evans & Dopita (1985) who have proposed that U is anti-correlated with abundance.

6.3. Reddening and Extinction

Figure 9 shows the radial variation of the extinction for each galaxy, as derived from the reddening of the Balmer decrement. Also shown are the extinction measures from MRS for their inner disk HII regions. A large dispersion in extinction can be seen over the face of these galaxies, clearly indicating the dominant effect of local variations over radial variations within the optical disk. Our derived extinctions for the two HII regions in common with MRS show deviations of ~ 1 magnitude, which may partly reflect variations in extinction over very small scales, accountable for by differences in pointing alone. Despite the large scatter which typifies the inner disk, clear evidence exists for diminished extinction at large radii. When account is made for the Galactic extinction towards these galaxies (indicated by the horizontal dashed line in Figure 9), the outer HII regions are consistent with internal extinctions of only $A_V \sim 0\text{--}0.2$ magnitudes.

We have used a weighted linear least-squares algorithm to fit the radial behaviour of the extinction in each galaxy and find $A_V = 1.73 - 1.07R/R_{25}$ (NGC 628), $0.95 - 0.46R/R_{25}$ (NGC 1058)

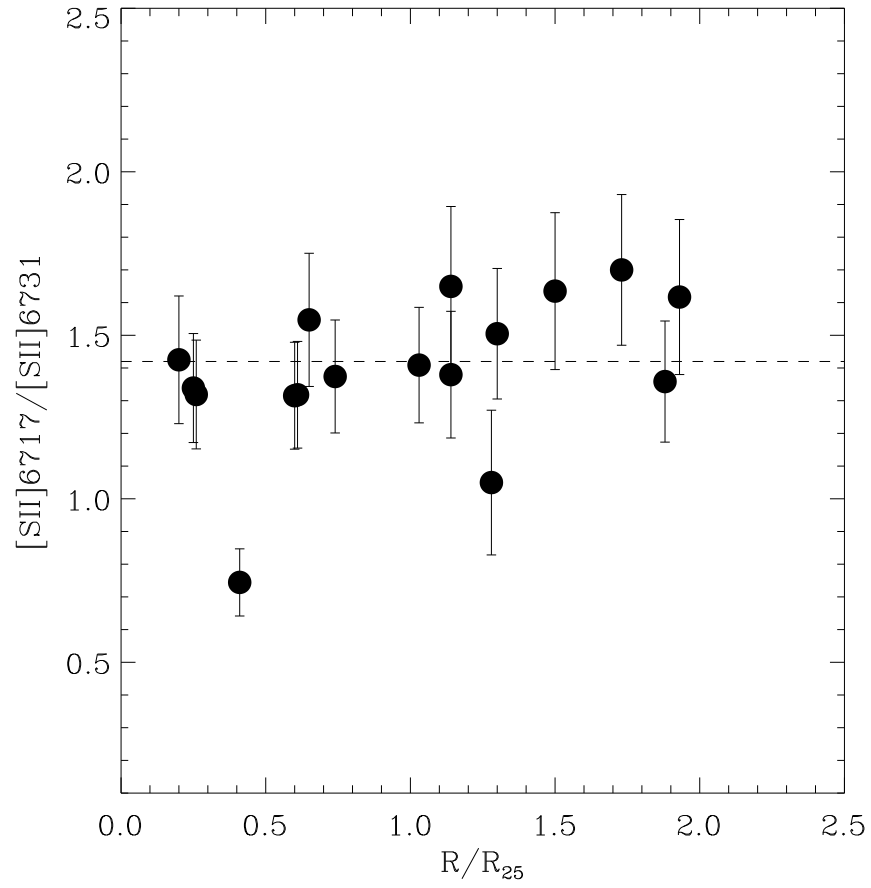


Fig. 7.— Variation of the density sensitive ratio, $[SII] \lambda 6717 / [SII] \lambda 6731$, for our entire sample of HII regions plotted as a function of radius, normalised to the size of the optical disk. The dashed line indicates the low density limit.

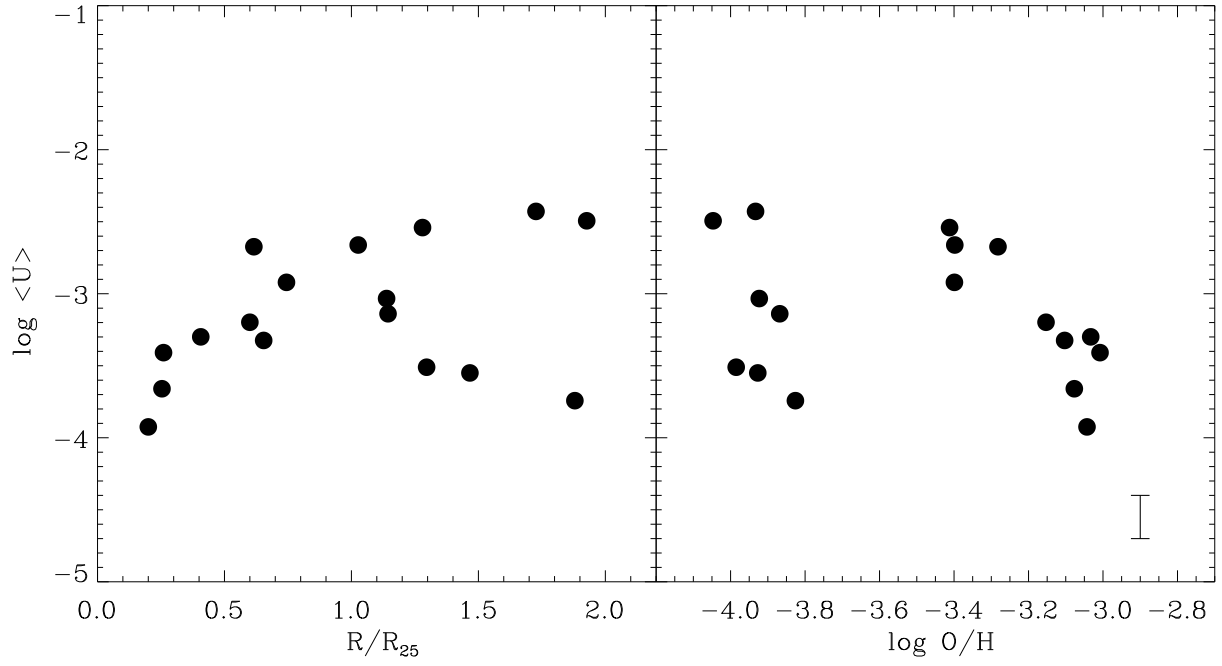


Fig. 8.— Variation of the volume-averaged ionization parameter, $\langle U \rangle$, for our entire sample of HII regions, plotted as a function of radius (right), normalised to the size of the optical disk, and as a function of oxygen abundance (left). The bar in the lower right corner indicates the probable error on these determinations.

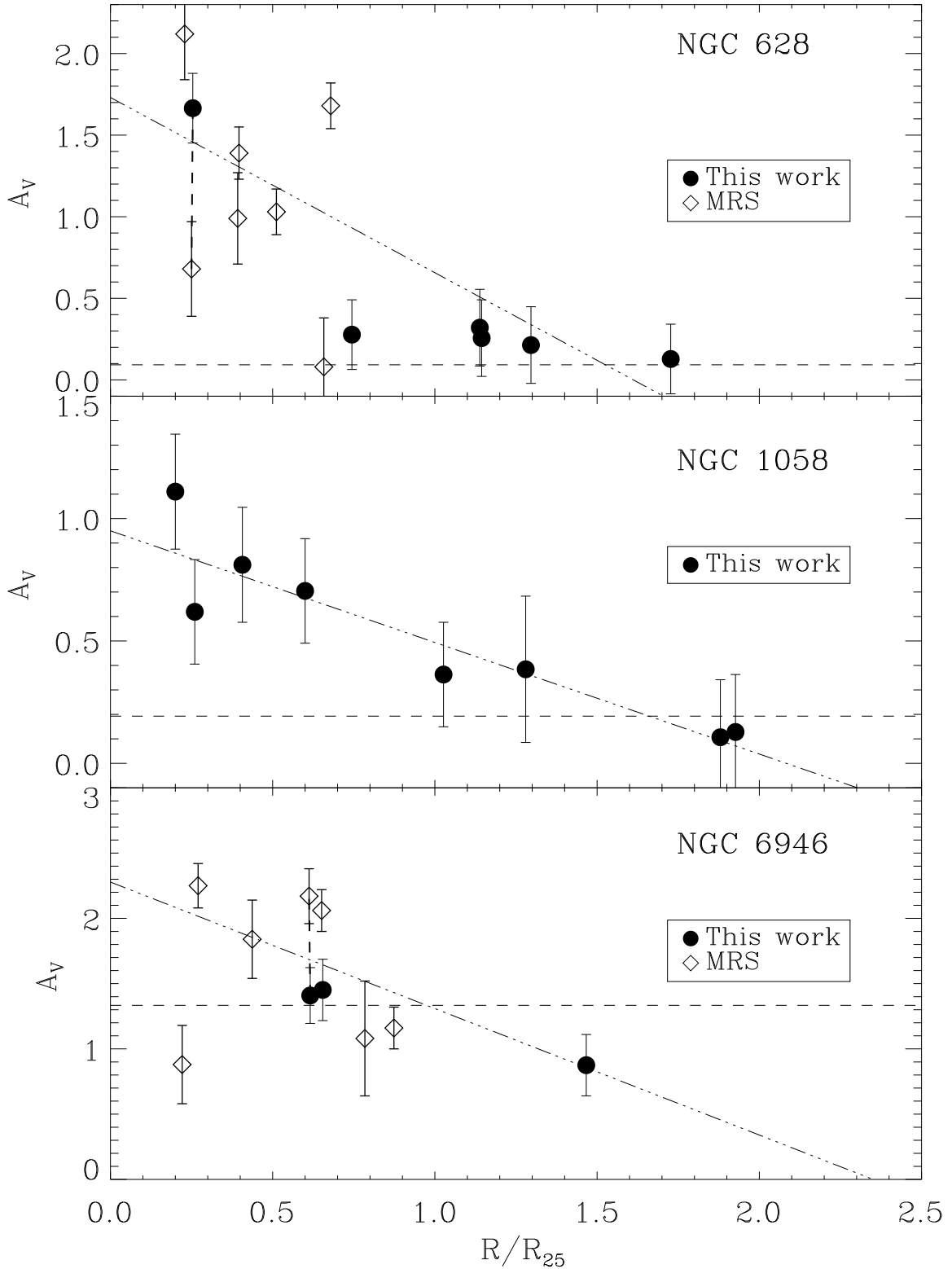


Fig. 9.— Radial variation of extinction for our galaxy sample, expressed in terms of the optical radius R_{25} . Our data points are indicated by filled circles, those from MRS are indicated by open diamonds. The horizontal dashed line indicates the level of Galactic extinction towards these galaxies, taken from the RC3. The dashed-dotted line indicates a linear least squares fit the points. Thick dashed lines join independent measurements of the same HII region.

and $2.28-0.97R/R_{25}$ (NGC 6946). Although clearly not an appropriate way to characterize the actual extinction in galactic disks, these parametrizations serve as a means to compare the global extinction properties of different galaxies. As can be seen, both the central value and the amplitudes of the gradients vary considerably from galaxy to galaxy. A radial gradient in extinction has also recently been detected in M101 by Kennicutt & Garnett (1996), but most previous studies have found evidence for only a very weak radial dependence. Our results suggest that this may be due in part to the limited radial coverage of such studies, which typically have sampled only the inner parts of galaxies where the amount of scatter dominates over any existing radial trend (eg. ZKH; MRS; Belley & Roy 1992; Scowen et al 1992). Interestingly, the radial gradients in A_V found here are comparable in magnitude to those found for the radial variation of the oxygen abundance (see below), lending support for the idea that the changes in A_V are driven largely by a decrease in available metals (see Table 7).

6.4. Oxygen

In Figure 10, we present the derived O/H abundances for the three galaxies in our sample as a function of the deprojected galactocentric radius, normalised to the optical radius. Since we have demonstrated that the dominant errors in the abundance determinations arise from the use of model calibrations and not from the measurements themselves, we omit placing formal error bars on the data points and instead place a representative error bar in each corner of the plot to indicate the estimated calibration uncertainty (± 0.2 dex) as derived above. Also shown are the abundances we derived using our present technique for the inner disk HII regions observed in NGC 628 and NGC 6946 by MRS (calculated from their published reddening-corrected line strengths). Our repeat measurements of the two MRS inner disk HII regions are indicated by a solid line which joins the independent measurements. As can be seen, there is an excellent agreement between these determinations.

Inner disk abundances typically range from 20% above solar to 40% below solar while beyond the edge of the optical disk, the measured oxygen abundances are $\sim 10-50\%$ solar. The outermost abundances in all three galaxies are $\sim 10-15\%$ solar, measured at radii in the range $1.5-2 R_{25}$. We have used a linear (uniformly-weighted) least squares routine to fit the variation of O/H as a function of deprojected galactocentric radius, expressed in terms of both the optical radius and in terms of kiloparsecs (see Table 7). We have also fit the gradients using only those points lying at or within the optical radius, in order to gauge the importance of the outer disk measurements in defining the abundance gradient. In this case, we find $\log(O/H)=-2.91-0.69(\pm 0.12)R/R_{25}$ (NGC 628), $-2.95-0.30(\pm 0.14)R/R_{25}$ (NGC 1058) and $-2.93-0.39(\pm 0.16)R/R_{25}$ (NGC 6946). These gradients are consistent with those derived for NGC 628 and NGC 6946 by ZKH, which were determined using weighted linear least-squares fits to only the inner disk samples of MRS and employing a different calibration of the O/H– R_{23} relationship than that which is adopted here. For comparison, they find gradients in units of the optical radius of $-0.96 (\pm 0.32)$ for NGC 628

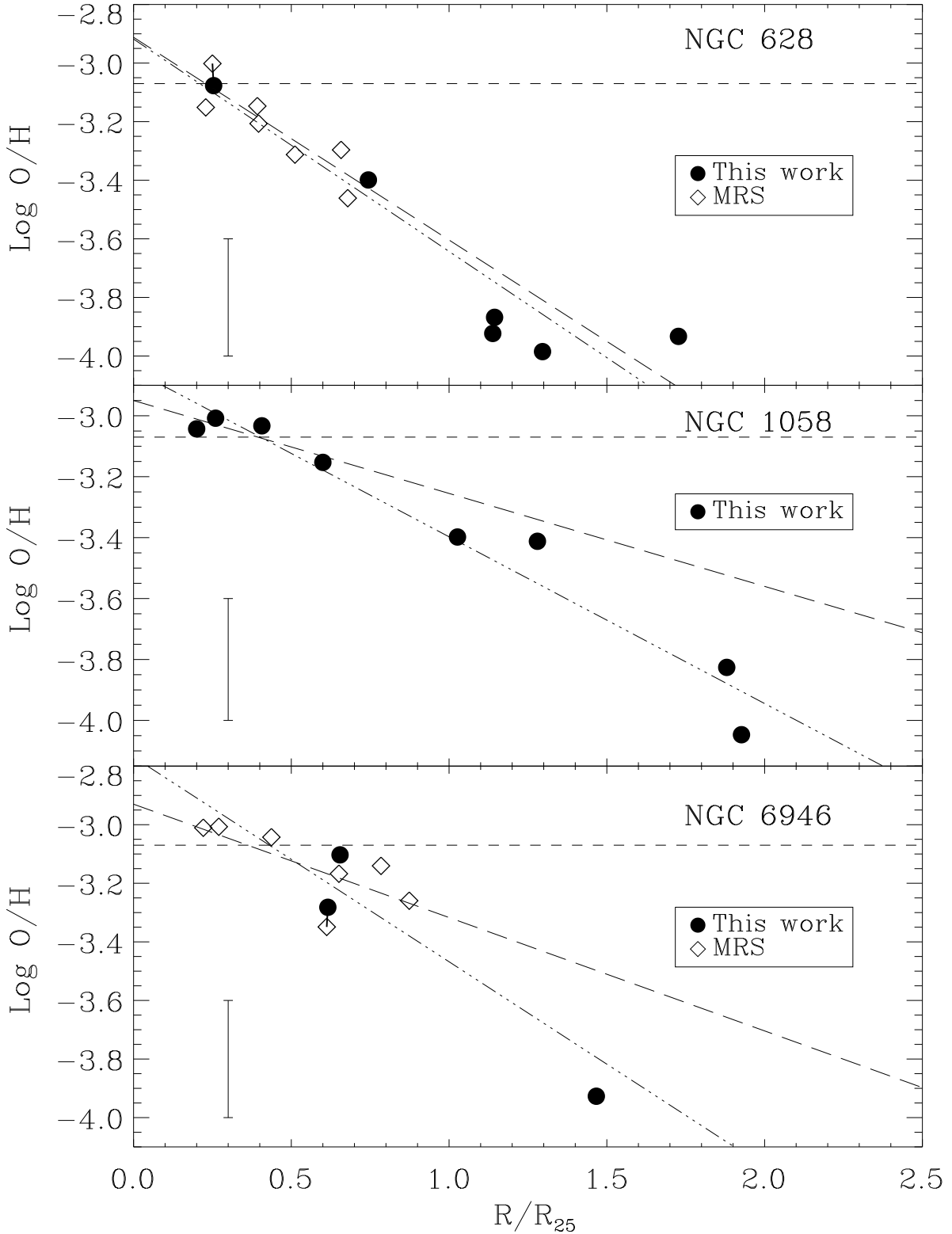


Fig. 10.— Radial variation of the oxygen abundance for our galaxy sample, expressed in terms of the optical radius R_{25} . Our abundance determinations are indicated by filled circles, and those taken from MRS are indicated by open diamonds. The horizontal dashed line indicates the solar abundance (Anders & Grevesse 1989). The dashed-dotted line indicates a linear least squares fit to all points, whereas the long dashed line indicates the fit to only those points lying within the

and $-0.55 (\pm 0.26)$ for NGC 6946. As is evident, the values of the outer disk abundances play a crucial role in defining the abundance gradient across the disk. Consideration of only inner disk abundances results in significantly flatter gradients for NGC 1058 and NGC 6946.

As we have discussed, a crucial aspect of the abundance determination via the semi-empirical method is determining whether a given HII region lies on the upper or lower branch of the calibration. Several of the extreme outer disk HII regions in our sample have values of $\log([\text{NII}]/[\text{OII}])$ close to unity, which makes the branch placement uncertain. In Figure 11, we show the effect of choosing the other branch in those cases in which the branch placement is somewhat ambiguous (defined here to be those cases where $\log([\text{NII}]/[\text{OII}])$ lies within ± 0.1 dex of -1). Only NGC 628 and NGC 1058 have HII regions which fall in this category. As can be seen, choice of the opposing branch for these HII regions can have a profound effect on the nature of the gradient, however it leads to rather strange (and unlikely) behaviours at large radii. We intend to obtain measures of $[\text{OIII}] \lambda 4363$ line, and thus the oxygen abundance via the ‘direct’ method, for those HII regions in which the abundance determination from the semi-empirical method is uncertain.

6.5. Nitrogen-to-Oxygen

Nitrogen-to-oxygen abundance ratios range from 50% above solar to 40% below solar across the inner disks, and from 20-50% solar beyond the optical radius (see Figure 12). The outermost regions have typical abundances of 20–25% solar. Linear least-squares (uniformly-weighted) fits have been carried out to characterize the radial behaviour (see Table 7). Fitting only those points lying at or within R_{25} produces gradients of $\log(\text{N/O}) = -0.74 - 0.76(\pm 0.13)R/R_{25}$ (NGC 628), $-0.97 - 0.02(\pm 0.36)R/R_{25}$ (NGC 1058) and $-0.72 - 0.40(\pm 0.09)R/R_{25}$ (NGC 6946). Once again, it can be seen that the outermost abundances play a key role in defining the abundance gradient. In particular, one might deduce no gradient in N/O if presented with only the inner disk measurements, whereas the outer disk measurements clearly show a decline in N/O at large radii.

7. Discussion

7.1. Constraining Outer Galactic Abundance Gradients

The results presented here constitute the largest set of extreme outer disk abundances ever measured, and probe the chemical abundance content of these optically faint, previously unexplored regions of present day galactic disks. We have found that the outermost HII regions studied have O/H abundances in the range of 10–15% solar and N/O abundances in the range of 20–25% solar. Such low abundances have rarely been measured before in spiral disks (eg. Garnett & Kennicutt 1994).

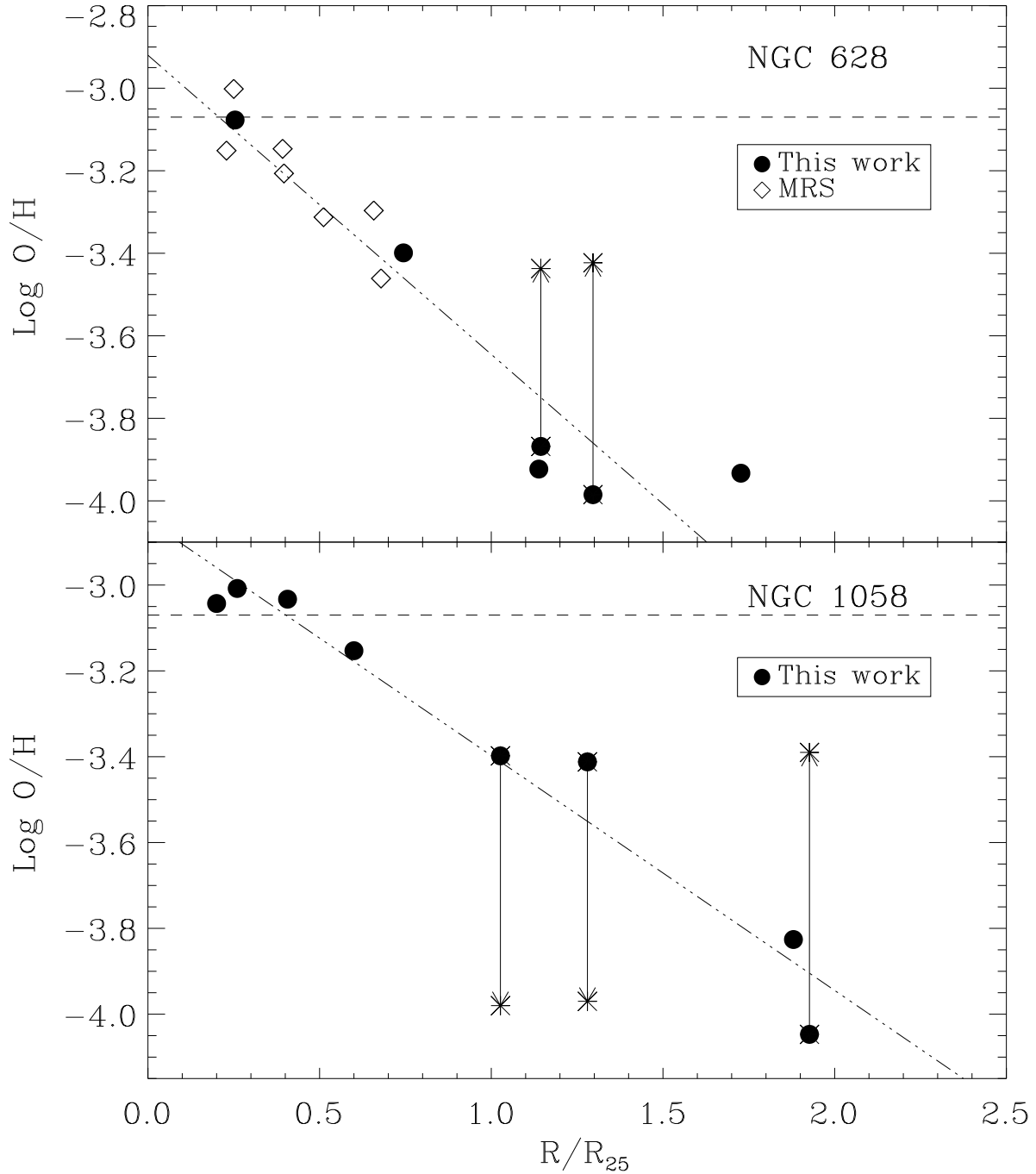


Fig. 11.— As in Figure 10, except we have explicitly indicated the change to the observed abundance gradients if the opposing branch is chosen for those HII regions where the placement is uncertain. The asterixes mark the new abundances for the HII regions in question.

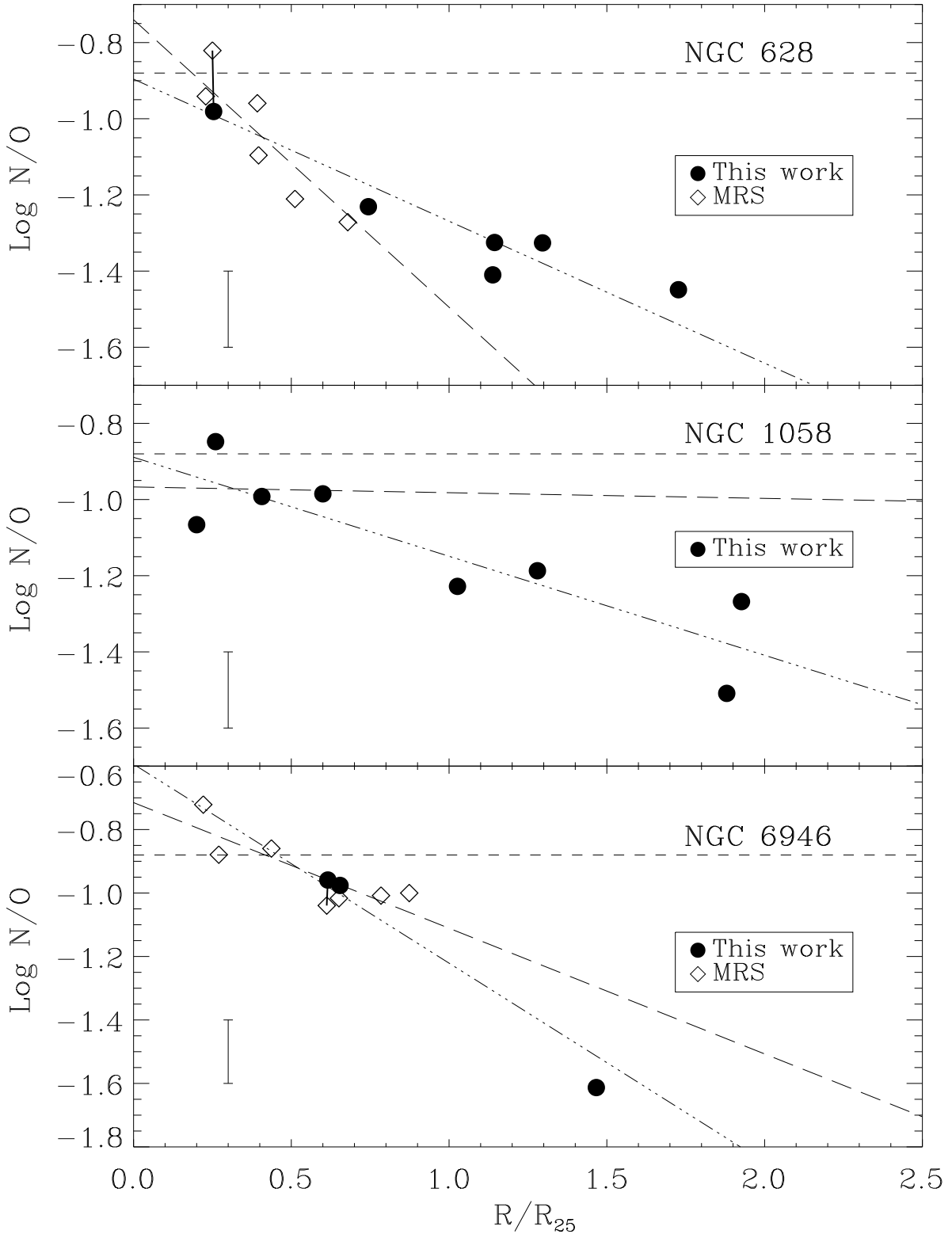


Fig. 12.— Radial variation of the nitrogen-to-oxygen abundance for our galaxy sample, expressed in terms of the optical radius R_{25} . Our abundances are indicated by filled circles, whereas those derived from MRS are indicated by open diamonds. The horizontal dashed line indicates the solar abundance (Anders & Grevesse 1989). The dashed-dotted line indicates a linear least squares fit to all points, whereas the long dashed line indicates the fit to only those points lying within the

We have shown that the outermost abundances play an important role in defining abundance gradients across the disks, and indeed often change the nature of the gradient. For example, in two of the galaxies studied here, the oxygen gradients are observed to steepen considerably when account is taken of the outermost HII regions. Within the limits of the current dataset, the radial abundance gradients are consistent with single log-linear relationships, although hints of interesting behaviour can be seen at large radii in two of the galaxies. There could be a flattening of the oxygen abundance beyond the edge of the optical disk in NGC 628 (although this result largely hinges on the metallicity of the outermost HII region), as well as a steepening of the outer gradient in NGC 1058. Unfortunately, given the relatively large errors in our abundance determinations, as well as the relatively small size of the current sample, it is not yet possible to assess the significance of these features. Similarly, it is not yet possible to constrain the amount of intrinsic scatter in the abundances as a function of galactocentric radius, which is of interest for understanding the efficiency and timescales for elemental mixing at large radii. While the two outermost HII regions in NGC 1058 show differences of $\gtrsim 0.2$ dex in both O/H and N/O despite lying at very similar radii, a knowledge of the electron temperatures of these regions will be required before we can distinguish between real scatter and uncertainties inherent in the model calibrations.

Chemical evolution models predict a variety of different behaviours for galactic abundance gradients (eg. Prantzos & Aubert 1995, Molla et al 1996, Wyse & Silk 1989, Clarke 1989). Of these models, some predict simple exponential declines while others produce steepenings or flattenings in the outer disk. Our current dataset is not yet sufficient to discriminate between various chemical evolution models, but we are continuing to obtain more and better data on these and other galaxies, spanning a range of physical environments and Hubble types.

7.2. Comparison to Other Galaxies

It is of great interest to compare our measurements of outer disk abundances with the few published measurements in the literature. High quality measurements exist for the Galaxy (Fich & Silkey 1991; Vilchez & Esteban 1996; Rudolph et al 1997; Afflerbach et al 1997), M81 (Garnett & Shields 1987) and M101 (Garnett & Kennicutt 1994), but these measurements do not extend to the extreme galactocentric radii that we have studied here.

In case of Galaxy, outer disk HII regions have been studied via optical and far-IR techniques out to $1.3R_{edge}$, where R_{edge} , the edge of the optical stellar disk, is taken to be 14 kpc (Ruphy et al 1997)⁷. Both Fich & Silkey (1991) and Vilchez & Esteban (1996) found evidence for flat gradients in the nitrogen abundance beyond the solar circle; additionally, Vilchez & Esteban (1996) found

⁷It remains unclear as to the relationship between the optical edge, as defined by star counts, and the 25th B-magnitude isophote.

evidence for only a mild outer gradient in oxygen abundance, with outer values of $\sim 20\%$ solar, and outer disk values of N/O consistent with those measured in the solar neighbourhood. More recently, Rudolph et al (1997) have re-examined outer abundance gradients using FIR lines for a sample of 5 HII regions. When combined with the results of other studies, these authors do not see compelling evidence for a flattening of the outer abundance gradients, and are able to fit the available data with single log-linear relationships. They caution, however, that their present sample is not yet sufficient to rule out the possible existence of a flattening of the abundance gradient in the outer Galaxy. They also find the variation of N/O throughout the Galactic disk to be consistent with a step function, with a mean $\log(\text{N/O})$ of -0.50 ± 0.02 for $R < 6.2$ kpc and, -0.83 ± 0.04 for $R > 6.2$ kpc. We note that HII regions have been discovered at much larger Galactocentric radii, out to ~ 28 kpc or $2R_{edge}$ (de Geus et al 1993) however no abundance determinations have been made for these as of yet.

In M81, the outermost HII region (lying at $\sim 1.3 R_{25}$) has an O/H abundance of roughly 20% solar, consistent with an extrapolation of the inner gradient, whereas the N/O abundance is close to solar and consistent with there being no gradient across the disk (Garnett & Shields 1987). On the other hand, the outermost HII region studied in M101 ($\sim 1.1 R_{25}$) has an O/H abundance of only 10% solar and an N/O abundance of 25% solar; both N/O and O/H are observed to decrease more or less smoothly with increasing galactocentric radius across the disk (Garnett & Kennicutt 1994). Curiously, these abundances are as low as those observed in the extremities of the galaxies studied here, despite that fact that we have probed the gas at significantly larger distances beyond the optical disk.

We find that the galaxies studied in the present work are more akin to M101 than the Galaxy or M81 since the outermost abundances of both O/H and N/O are observed to decrease more or less smoothly across their disks. The striking difference between the level of N/O enrichment seen in the outer disks of galaxies studied here (and M101) and in the outer disks of the Galaxy and M81 is particularly puzzling and clearly warrants further study.

7.3. Implications for Understanding the Evolution of Galactic Disks

Our outer disk measurements are largely consistent with those observed in other low gas surface density objects, such as gas-rich dwarf irregulars (eg. Garnett 1990; Skillman et al 1989; Skillman et al 1997; Thuan et al 1995; Miller & Hodge 1996)⁸ and some low surface brightness galaxies (McGaugh 1994). It has often been suggested that outer galactic disks are ‘built’ up through the accretion of gas, either smoothly (eg. Gunn & Gott 1972; Larson 1976) or as gas-rich

⁸Note however that the measured outer disk metallicities are still considerably in excess of the most metal poor, gas-rich objects known locally, eg. IZw18, UGC4483 and SBS 0335-052. These objects have O/H abundances of only 2–3% solar (eg. Skillman & Kennicutt 1993, Skillman et al 1994, Izotov et al 1997), even although there is evidence for moderately long periods ($\gtrsim 10$ Myr) of star formation in at least one case (eg. Garnett et al 1997b).

low mass companions (eg. White & Rees 1987; Kauffman et al 1993; Kamphuis 1993; Zaritsky 1995). There would appear to be no obvious argument against this hypothesis on the basis of chemical abundance content alone.

On the other hand, one might consider the scenario in which outer galactic disks evolve in relative isolation, with little inflow or outflow. The simple ‘closed box’ model of Schmidt (1963) can be used to predict the mean metallicity expected for such regions, under the assumption of instantaneous recycling (appropriate for oxygen). The closed box model can be represented by a simple relation (Searle & Sargent (1972))

$$Z = -p \ln \mu$$

where p is the yield of the element in question and μ is the gas fraction, defined as baryonic mass in gas to the total baryonic mass (stars + gas). Our deep B-band surface photometry yields B-band surface brightnesses at two optical radii of $\sim 0.1 L_{\odot} \text{ pc}^{-2}$ in NGC 628 and NGC 6946 and $\sim 1.2 L_{\odot} \text{ pc}^{-2}$ in NGC 1058 (Ferguson et al 1998b). Under the assumption of $M/L \sim 2$, this leads to surface mass densities of 0.2 and 2.4 $M_{\odot} \text{ pc}^{-2}$. The B-band M/L ratio is sensitive to the star formation history of the outer disk, but is unlikely to be too much larger than the adopted value, which is found for the solar neighbourhood (Kuijken & Gilmore 1989). Inspection of the HI maps of these galaxies reveals typical HI surface densities of $\sim 1 M_{\odot} \text{ pc}^{-2}$ (NGC 628) to $\sim 3 M_{\odot} \text{ pc}^{-2}$ (NGC 1058, NGC 6946) in the extreme outer disks (van der Kruit & Shostak 1984, Shostak & van der Kruit 1984, Kamphuis 1993). Correcting for helium (a factor of 1.3), we derive gas fractions of ~ 0.6 in NGC 1058 and ~ 0.90 in NGC 628, NGC 6946. Adopting a yield of $0.5 Z_{\odot}$, consistent with the observed mean metallicity of stars in the solar neighbourhood (Wyse & Gilmore 1995), the simple model then predicts oxygen abundances of 6% solar for NGC 628, 25% solar for NGC 1058 and 2% solar for NGC 6946. These values can be compared to the observed metallicities of 10–15% solar. Despite the many uncertainties involved, both NGC 628 and NGC 1058 have metallicities which lie within a factor of two of the closed-box model predictions, thus suggesting that the role of gas flows in the evolution of their outer disks is similar to that for the solar neighbourhood. The outer disk of NGC 6946, on the other hand, does not appear to fit this picture. In the future, we plan to investigate the predictions of the simple model in more detail, including study of the radial variation in the derived effective yield.

7.4. Comparison to High Redshift Damped Lyman- α Systems

Much recent attention has been focused on uncovering the nature of the damped Ly α systems (DLAs) which cause absorption in the spectra of high redshift quasars. While there remains much debate on this topic, follow-up imaging and spectroscopy of these systems lends support for the idea that at least some of them are young disk galaxies (eg. Wolfe 1988; Briggs et al 1989; Djorgovski et al 1996). The distribution of impact parameters for these systems is not well-defined; however, in the particular case of Djorgovski et al (1996), an impact parameter of

18 kpc is inferred which clearly places the line-of-sight in the outer parts of what appears to be a large disk galaxy at $z=3.15$. How do the chemical abundances measured in the DLAs compare to those measured in the extended parts of local disk galaxies? There have been many recent efforts to measure the gas-phase chemical abundances in DLA systems (eg. Pettini et al 1994, 1995, 1997; Wolfe et al 1995; Lu et al 1996, 1998); studies have generally found them to exhibit a wide range of low metallicities, ranging from less than 1/100th of the solar value to 1/10th solar, and showing a trend of increasing metallicity with decreasing redshift, albeit with considerable scatter at all redshifts (eg. Lu et al 1996, Pettini et al 1997). Pettini et al (1997) calculate a column density-weighted mean metallicity of 1/13th solar for their sample of 34 DLAs ($0.7 < z < 3.4$), using the Zn lines which should be relatively unaffected by depletion onto dust.⁹ This comparison suggests an intriguing similarity in the mean chemical enrichment level of DLA systems and present-day outer galactic disks, with DLA systems being only slightly more metal poor.

Figure 13 shows a a plot of nitrogen-to-oxygen abundance as a function of O/H for our present sample of HII regions, as well as those inner disk regions from MRS. We have indicated where IZw18, the most metal poor gas-rich object in the local Universe, falls on this diagram (Skillman & Kennicutt 1993). Also shown are a set of N/Si measurements (or upper limits) for a sample of 15 DLA systems with $z > 2$ from Lu et al (1998). These authors argue that N/Si is equivalent to N/O, under the assumption that O/Si is approximately solar in DLA systems and that dust depletion is not significant. This plot reveals that while many DLA systems in the Lu et al sample are considerably more metal poor than present-day outer galactic disks, others are only slightly displaced from outer disks in terms of O/H and almost identical in terms of N/O. The long dynamical timescales ($\sim 10^8$ – 10^9 years) which characterize the extreme outer disks imply that they evolve at a very slow rate but, nonetheless, we would expect them to have been more metal poor in the past than at the present epoch. We therefore conclude that while, on average, DLA systems tend to be slightly more metal poor than outer galactic disks at present, the two were very likely indistinguishable at large lookback times.

7.5. The Origin of Nitrogen

A major unsolved question is the importance of primary and secondary processes in the production of nitrogen. Nitrogen is believed to be mostly a product of secondary nucleosynthesis, being produced via the CNO cycle, however it is also thought to have primary component which can be produced in the earlier helium burning stages (Renzini & Voli 1981). It is thought that secondary nitrogen is produced by stars of a wide range of masses whereas primary nitrogen is produced by only intermediate mass stars ($4 \lesssim M/M_{\odot} \lesssim 8$) (Renzini & Voli 1981, Matteucci 1986); there is evidence however that nitrogen produced in massive stars is also predominantly

⁹Note that the average HI column for this sample of DLA systems is roughly 10^{21} cm^{-2} , which is several times higher than the typical HI column where our sample of outer HII regions reside (a few times 10^{20} cm^{-2}).

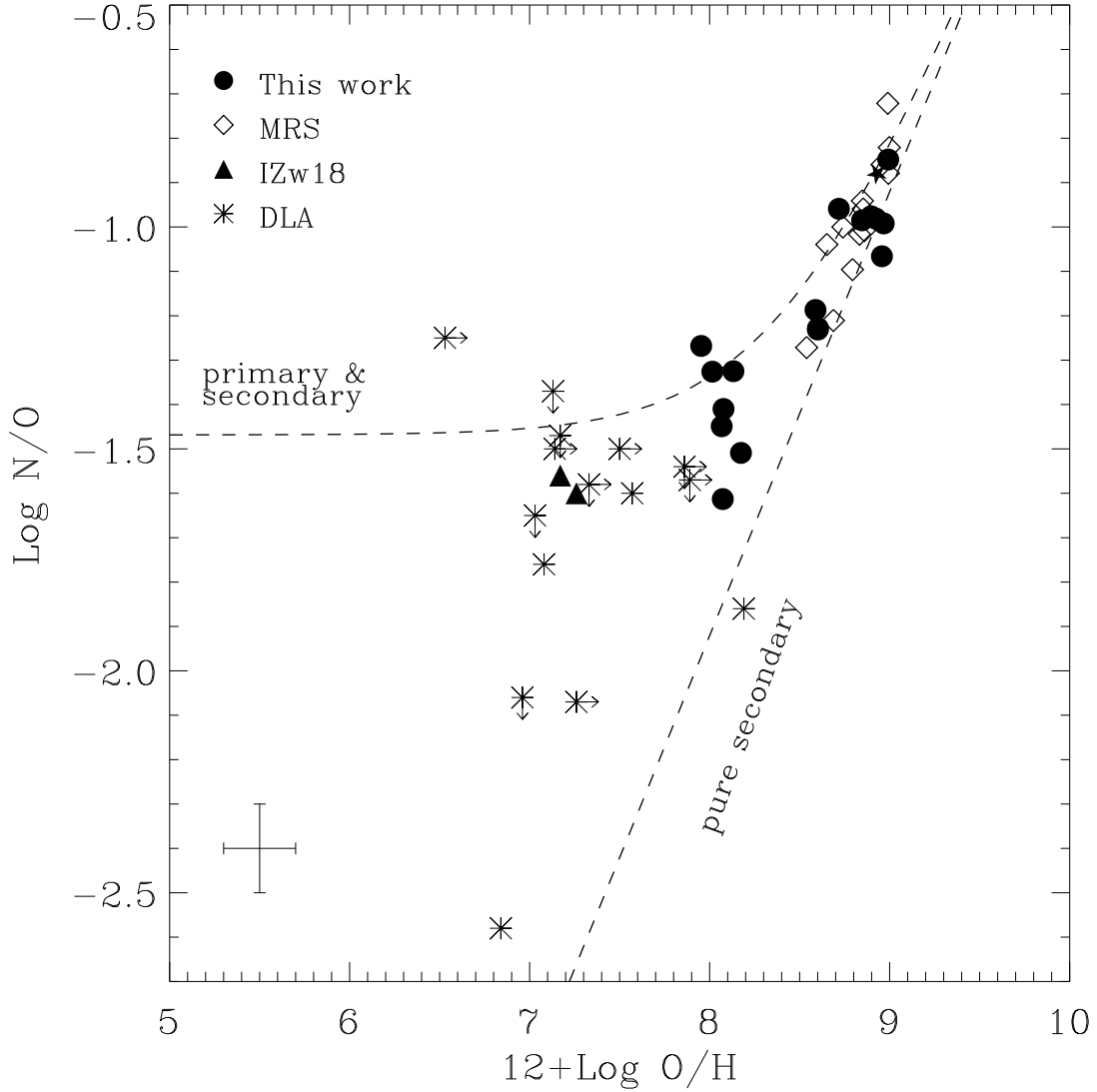


Fig. 13.— Variation of $\log(N/O)$ vs $12 + \log(O/H)$ for our sample of HII regions, as well as the inner disk HII regions measured by MRS. Typical uncertainties in our measurements are indicated by the error bar in the lower left. The location of the Sun in this diagram is indicated by a solid star. We also plot values for the most metal poor object known in the local Universe, IZw18 (Skillman & Kennicutt 1993), as well as the N/Si and Si/H measurements for a sample of high redshift DLA systems from Lu et al (1998). (Note we have not shown the error bars for these data, but only the upper and lower limits). The dashed curves indicate the expectations for a pure secondary and primary+secondary origins for nitrogen from Vila-Costas & Edmunds (1993). The extreme outer disk HII regions are consistent with a combination of both primary and secondary production of nitrogen.

primary. As an example, Laird (1985) finds that $[N/Fe]$ is constant for solar-neighbourhood stars with $-1.8 \leq [Fe/H] \leq 0.5$, implying that nitrogen and iron are produced in the same way, by the same stars. Since it is well known that some iron is primary, and produced on short timescales by Type II supernovae from the core-collapse of massive stars (eg. Arnett 1995), then one expects that such stars must also contribute to nitrogen production. The simple model for the chemical evolution of galaxies (ie. closed box) predicts that N/O will be independent of O/H for a primary origin of nitrogen, and proportional to O/H for a secondary origin (see Vila-Costas & Edmunds 1993 for a discussion, including the complication of ‘delayed’ primary production).

The timescales for nitrogen production differ in stars of varying mass. If nitrogen is predominantly produced by massive stars, then there should be no time delay between the release of the element with respect to oxygen, and thus one expects the N/O ratio to exhibit only a small amount of scatter. If, on the other hand, most nitrogen comes from intermediate mass stars, then one expects a time delay of up to a few times 10^8 years between the release of N/O . This is expected to introduce a large scatter in the N/O ratio at low O/H , decreasing with increasing metallicity as the effects of the time delay become less and less important (eg. Garnett 1990; Pilyugin 1992).

In Figure 13, we have overplotted the expectations for primary and secondary production of nitrogen, as taken from Vila-Costas & Edmunds (1993). At high metallicities, the expected linear trend between O/H and N/O is seen, indicative of the dominant role of secondary nitrogen production. On the other hand, the extreme outer disk HII regions are seen to populate the region bracketed by the pure secondary and primary + secondary curves, and thus appear consistent with a combination of primary and secondary production of nitrogen. The spread in N/O at fixed O/H in the outer disk may very well reflect the timescale between ‘bursts’ of star formation, produced perhaps by the passage of a spiral arm. Further measurements, with improved accuracy, are needed to better understand these results.

8. Summary and Future Work

We have presented the first results from a systematic study of the physical properties and chemical abundances in a sample of newly-discovered, extreme outer disk HII regions. Optical spectra are presented for HII regions in three, late-type spirals – NGC 628, NGC 1058 and NGC 6946 – all of which are characterized by large than average HI-to-optical sizes. We have found that the outermost HII regions studied, typically lying at $1.5-2R_{25}$, have O/H abundances in the range of 9–15% solar and N/O abundances in the range of 20–25% solar. Evidence is also found for diminished dust extinction at large radii, with the outermost HII regions having internal extinctions of $A_V \sim 0-0.2$. Electron densities in the outer disk HII regions are comparable to those found in the inner disk. The outer disk HII regions are observed to span a range in volume-averaged ionization parameter $\langle U \rangle$, and no correlation is seen with either galactocentric radius or metallicity.

By combining our sample of outer disk measurements with those for inner disk HII regions published in the literature, we have been able to probe the radial variation of both oxygen and nitrogen-to-oxygen abundances out to unprecedented radii. Single log-linear relationships are found to adequately describe the radial abundance variations, although the derived slopes often differ considerably from those found if only inner disk HII regions are used to define the fit. The small number of HII regions in our present sample, together with uncertainties in the calibrations of the semi-empirical methods used here to determine abundances, limit the ability to constrain both subtle changes in the radial gradient as well as scatter in the outer disk.

Comparison of our outermost oxygen abundances with the predictions of the simple closed-box model for chemical evolution reveals a general consistency for two of the three galaxies, and suggests that the role of gas flows in the evolution of their extreme outer disks is comparable to that in the solar neighbourhood. An intriguing similarity is found between both the mean enrichment level and the nitrogen-to-oxygen abundance in outer disks and in some high redshift DLA systems, implying that outer disks at the present epoch are relatively unevolved systems. While DLA systems tend to be slightly more metal poor than present-day outer disks, they were very likely indistinguishable at large lookback times. Finally, we have found that the outer disk HII regions in our sample are consistent with both primary and secondary production of nitrogen.

A limitation of the current work is the reliance on semi-empirical methods to determine the abundances. A concern is that the outer disk HII regions under study here are physically different from the clusters of OB stars on which the model calibrations are based. A more complete set of photoionization models, extending to HII regions which are ionized by only a few massive stars, would be highly desirable. We are intending to measure the temperature-sensitive [OIII] $\lambda 4363$ line, or at least place strong limits on it, for several of the brightest HII regions in the present sample, in order to compare the ‘direct’ and semi-empirical abundance determinations for these objects. We are also continuing to obtain measurements of additional HII regions in these galaxies, as well as extending our work to include several other galaxies, residing in a range of physical environments (eg. field and cluster). The new generation of 8-m telescopes will significantly ease the task of measuring abundances for extreme outer disk HII regions, while future HST instruments will make it possible to routinely probe outer disk abundances via quasar absorption lines. A larger sample of outer disk abundances will make it possible to study the detailed nature of the abundance gradient at large radii, as well as the amount of intrinsic scatter at a fixed radius. Ultimately, we will use our measurements of outer disk chemical abundances, along with our measurements of past and present star formation rates, in order to construct self-consistent models of outer disk evolution.

We thank Stacy McGaugh for providing the grid reproduced in Figure 5 and for many useful discussions concerning his model calibrations. We thank Deidre Hunter, Tim Heckman, Roberto Terlevich and Max Pettini for interesting discussions and suggestions at various stages of this project. AMNF acknowledges support from an Amelia Earhart Fellowship from Zonta

International. JSG has been partially supported by JPL through the WFPC2 Investigation Definition Team under NASA contract NAS 7-1260. RFGW acknowledges support from NASA grant NAGW-2892.

REFERENCES

- Afflerbach, A., Churchwell, E. & Werner, M. W. 1997, *ApJ*, 478, 190
- Anders, N. & Grevesse, E. 1989, *Geochim. Cosmochim. Acta*, 53, 197
- Arnett, D. 1995, *ARA&A*, 33, 115
- Belley, J. & Roy, J.-R. 1992, *ApJS*, 78, 61
- Bingelli, B., Tamman, G. A. & Sandage, A. 1987, *AJ*, 94, 251
- Briggs, F., Wolfe, A. M., Liszt, H., Davis, M. M. & Turner, K. L. 1989, *ApJ*, 341, 650
- Broeils, A. 1994, Ph. D. Thesis, Groningen University
- Cayatte, V., Kotanyi, C., Balkowski, C. & van Gorkam, J. H. 1994, *AJ*, 107, 1003
- Clarke, C. J. 1989, *MNRAS*, 238, 283
- Czyzak, S. J., Keyes, C. D. & Aller, L. H. 1986, *ApJS*, 61, 159
- De Geus, E. J., Vogel, S. N., Digel, S. W. & Gruendl, R. A. 1993, *ApJ*, 413, L97
- de Robertis, M. M., Dufour, R. J. & Hunt, R. W. 1987, *JRASC*, 85, 195
- de Vaucouleurs, G., de Vaucouleurs, A., Corwin, H. R., Buta, R. J., Paturel, G., & Fouqu e, P. 1991, *Third Reference Catalogue of Bright Galaxies* (Springer-Verlag, New York) (RC3)
- Dickey, J. M., Hanson, M. & Helou, G. 1990, *ApJ*, 352, 522
- Djorgovski, S. G., Pahre, M. A., Bechtold, J. & Elston, R. 1996, *Nature*, 382, 234
- Dopita, M. A. & Evans, I. N. 1986, *ApJ*, 307, 431
- Edmunds, M. G. & Pagel, B. E. J. 1984, *MNRAS*, 211, 507
- Evans, I. N. & Dopita, M. A. 1985, *ApJS*, 58, 125
- Ferguson, A. M. N., Wyse, R. F. G., Gallagher, J. S. & Hunter, D. A. 1996a, *AJ*, 111, 2265
- Ferguson, A. M. N., Wyse, R. F. G. & Gallagher, J. S. 1996b, *AJ*, 112, 2567
- Ferguson, A. M. N. 1997, Ph. D. Thesis, Johns Hopkins University.
- Ferguson, A. M. N., Wyse, R. F. G., Gallagher, J. S. & Hunter, D. A. 1998a, *ApJL*, submitted.
- Ferguson, A. M. N., Wyse, R. F. G., Gallagher, J. S. & Hunter, D. A. 1998b, in preparation.
- Fich, M. & Silkey, M. 1991, *ApJ*, 366, 107

- Garnett, D. R. 1990, *ApJ*, 363, 142
- Garnett, D. R. & Shields, G. A. 1987, *ApJ*, 317, 82
- Garnett, D. R., Odewahn, S. C. & Skillman, E. D. 1992, *AJ*, 104, 1714
- Garnett, D. R. & Kennicutt, R. C. 1994, *ApJ*, 426, 123
- Garnett, D. R., Shields, G. A., Skillman, E. D., Sagan, S. P. & Dufour, R. J. 1997a, *ApJ*, 489, 63
- Garnett, D. R., Skillman, E. D., Dufour, R. J. & Shields, G. A. 1997b, *ApJ*, 481, 174
- Gunn, J. & Gott, J. R. 1972, *ApJ*, 176, 1
- Hodge, P. & Kennicutt, R. C. 1983, *AJ*, 88, 296
- Howarth, I. 1983, *MNRAS*, 203, 301
- Izotov, Y. I., Thuan, T. T. & Lipovetsky, V. A. 1994, *ApJ*, 435, 647
- Kamphuis, J. 1993, Ph. D. Thesis, Groningen University
- Kauffmann, G., White, S. D. M. & Guiderdoni, B. 1993, *MNRAS*, 264, 201
- Kennicutt, R. C. & Garnett, D. R. 1996, *ApJ*, 456, 504
- Kuijken, K. & Gilmore, G. 1989, *MNRAS*, 239, 605
- Laird, J. B. 1985, *ApJ*, 289, 556
- Larson, R. B. 1976, *MNRAS*, 176, 1
- Lu, L., Sargent, W. L., Barlow, T. A., Churchill, C. W. & Vogt, S. S. 1996, *ApJS*, 107, 475
- Lu, L., Sargent, W. L. & Barlow, T. A. 1998, *AJ*, 115, 55
- Massey, P., Strobel, K., Barnes, J. V. & Anderson, E. 1988, *ApJ*, 328, 315
- Matteucci, F. 1986, *MNRAS*, 211, 911
- McCall, M. L., Rybski, P. M. & Shields, G. A. 1984, *ApJS*, 57, 1 (MRS)
- McGaugh, S. S. 1991, *ApJ*, 380, 140
- McGaugh, S. S. 1994, *ApJ*, 426, 135
- Mendoza, C. & Zeppen, C. J. 1982, *MNRAS*, 198, 127
- Miller, B. W. 1994, Ph. D. Thesis, University of Washington
- Miller, B. W. & Hodge, P. 1996, *ApJ*, 458, 467

- Molla, M., Ferrini, F. & Diaz, A. I. 1996, *ApJ*, 466, 668
- Nussbaumer, H. & Storey, P. J. 1981, *A&A*, 96, 91
- Oey, M. S. & Kennicutt, R. C. 1993, *ApJ*, 411, 1370
- Osterbrock, D. E. 1989, *Astrophysics of Gaseous Nebulae and Active Galactic Nuclei* (Mill Valley: University Science Books)
- Pagel, B. E. J., Edmunds, M. G., Blackwell, D. E., Chun, M. S. & Smith, G. 1979, *MNRAS*, 189, 95
- Pagel, B. E. J., Edmunds, M. G. & Smith, G. 1980, *MNRAS*, 193, 219
- Pagel, B. E. G. & Edmunds, M. G. 1981, *ARA&A*, 2, 77
- Pettini, M., Smith, L. J., Hunstead, R. W. & King, D. L. 1994, *ApJ*, 426, 79
- Pettini, M., Lipman, K., & Hunstead, R. W. 1995, *ApJ*, 451, 100
- Pettini, M., Smith, L. J., King, D. L. & Hunstead, R. W. 1997, *ApJ*, 486, 665
- Pickering, T., Impey, C., van Gorkom, J. & Bothun, G. 197, *AJ*, 114, 1858
- Pilyugin, L. 1992, *A&A*, 260, 58
- Prantzos, N. & Aubert, O. 1995, *A&A*, 302, 69
- Renzini, A. & Voli, M. 1981, *A&A*, 94, 175
- Rudolph, A. L., Simpson, J. P., Haas, M. R., Erickson, E. F. & Fich, M. 1997, *ApJ*, 489, 94
- Ruphy, S., Robin, A. C., Epchtein, N., Copet, E., Bertin, E., Fouque, P. & Gugliemo, F. 1996, *A&A*, 313, 21
- Schechter, P. L. 1980, *AJ*, 85, 801
- Schild, R. E. 1977, *AJ*, 82, 337
- Schmidt, M. 1963, *ApJ*, 137, 758
- Scowen, P. A., Dufour, R. J. & Hester, J. J. 1992, *AJ*, 104, 92
- Searle, L. 1971, *ApJ*, 168, 327
- Searle, L. & Sargent, W. L. W. 1972, *ApJ*, 173, 25
- Seaton, M. J. 1979, *MNRAS*, 185, 57
- Shields, G. A. 1974, *ApJ*, 193, 335

- Shields, J. C. & Kennicutt, R. C. 1995, *ApJ*, 454, 807
- Shostak, G. S. & van der Kruit, P. C. 1984, *A&A*, 132, 20
- Skillman, E. D. 1989, *ApJ*, 347, 883
- Skillman, E. D., Kennicutt, R. C. & Hodge, P. W. 1989, *ApJ*, 347, 875
- Skillman, E. D., Terlevich, R. J., Kennicutt, R. C., Garnett, D. R. & Terlevich, E. 1994, *ApJ*, 431, 172
- Skillman, E. D. & Kennicutt, R. C. 1993, *ApJ*, 411, 655
- Skillman, E. D., Bomans, D. J. & Kobulnicky, H. A. 1997, *ApJ*, 474, 205
- Thuan, T., Izotov, Y. I. & Lipovetsky, V. A. 1995, *ApJ*, 445, 108
- Thurston, T. R., Edmunds, M. G. & Henry, R. B. C. 1996, *MNRAS*, 283, 990
- Vacca, W. D., Garmany, C. D. & Shull, J. M. 1996, *ApJ*, 460, 914
- van der Kruit, P. C. & Shostak, G. S. 1984, *A&A*, 134, 258
- Vila-Costas, M. B. & Edmunds, M. G. 1992, *MNRAS*, 259, 121
- Vila-Costas, M. B. & Edmunds, M. G. 1993, *MNRAS*, 265, 199
- Vilchez, J. M., Pagel, B. E. J., Diaz, A. I., Terlevich, E. & Edmunds, M. G. 1988, *MNRAS*, 235, 633
- Vilchez, J. M. & Esteban, C. 1996, *MNRAS*, 280, 720
- Webster, B. L. & Smith, M. G. 1983, *MNRAS*, 204, 743
- White, S. D. M. & Rees, M. J. 1987, *MNRAS*, 183, 341
- Wolfe, A. 1988 in *Quasar Absorption Lines*, eds. J. C. Blades, D. Turnshek & C. A. Norman (Cambridge University Press), p. 297
- Wolfe, A. M., Lanzetta, K. M., Foltz, C. B. & Chaffee, F. H. 1995, *ApJ*, 454, 698
- Wyse, R. F. G. & Silk, J. 1989, *ApJ*, 339, 700
- Wyse, R. F. G. & Gilmore, G. 1995, *AJ*, 110, 2771
- Zaritsky, D., Kennicutt, R. C., & Huchra, J. P. 1994, *ApJ*, 420, 558 (ZKH)
- Zaritsky, D. 1995, *ApJ*, 448, L17

This figure "ferguson.fig1.jpg" is available in "jpg" format from:

<http://arxiv.org/ps/astro-ph/9805166v1>

TABLE 1. Galaxy Properties

Object	NGC 628	NGC 1058	NGC 6946	Refs
Type	SA(s)c	SA(rs)c	SAB(rs)cd	1
Adopted D (Mpc)	10.7	10.0	5.3	2
M_B	-20.4	-18.5	-20.8	3
R_{25} (')	5.2	1.5	5.7	1
R_{25} (kpc)	16.2	4.4	8.8	1
R_{HI}/R_{25}	2.3	3.1	2.8	4
SFR (M_{\odot}/yr)	4.6	0.35	2.0	5

References for Table 1.

(1) from RC3; de Vaucouleurs et al. (1991); (2) distances are calculated from the heliocentric velocities through use of the linear Virgocentric infall model of Schechter (1980) with parameters $\gamma = 2$, $V_{virgo}=976 \text{ km s}^{-1}$, $\omega_{\odot}=220 \text{ km s}^{-1}$ (Binggelli et al 1987) and $D_{virgo}=15.9 \text{ Mpc}$ (i.e. $H_o=75 \text{ km s}^{-1} \text{ Mpc}^{-1}$); (3) derived from B_T^0 as provided in the RC3, assuming the adopted distance; (4) values for NGC 628 and NGC 6946 are taken from Cayette et al (1994), adjusting to the values of R_{25} adopted here; value for NGC 1058 derived from Dickey et al (1990). R_{HI} is calculated to be the radius at which the HI column density has fallen to 10^{20} cm^{-2} ; (5) Ferguson et al (1998a).

This figure "ferguson.fig2.jpg" is available in "jpg" format from:

<http://arxiv.org/ps/astro-ph/9805166v1>

TABLE 2. Properties of Observed HII Regions

Our ID (1)	Other IDs (2)	R/R ₂₅ (3)	D(pc) (4)	F(H α) (5)	L(H α) (6)	N(O5V) (7)
FGW 628-A	MRS(N0628(-074-022)), HK451	0.25	970	1.8×10^{-13}	2.4×10^{39}	52
FGW 628-B	HK330	0.74	1500	1.9×10^{-13}	2.6×10^{39}	57
FGW 628-C	...	1.14	360	7.5×10^{-15}	1.0×10^{38}	2
FGW 628-D	...	1.14	290	6.1×10^{-15}	8.3×10^{37}	2
FGW 628-E	...	1.30	430	1.1×10^{-14}	1.5×10^{38}	3
FGW 628-F	...	1.73	470	1.9×10^{-14}	2.7×10^{38}	6
FGW 1058-A	...	0.20	700	8.2×10^{-14}	9.8×10^{38}	21
FGW 1058-B	...	0.26	240	3.0×10^{-14}	3.6×10^{38}	8
FGW 1058-C	...	0.41	550	5.7×10^{-14}	6.9×10^{38}	15
FGW 1058-D	...	0.60	410	4.3×10^{-14}	5.1×10^{38}	11
FGW 1058-E	...	1.03	550	6.8×10^{-14}	8.1×10^{38}	18
FGW 1058-F	...	1.28	170	1.8×10^{-15}	2.1×10^{37}	1
FGW 1058-G	...	1.88	360	5.9×10^{-15}	7.1×10^{37}	2
FGW 1058-H	...	1.93	260	5.8×10^{-15}	6.9×10^{37}	2
FGW 6946-A	MRS(N6946(+182+103)), HK29	0.61	460	3.4×10^{-13}	1.1×10^{39}	25
FGW 6946-B	HK16	0.65	370	2.1×10^{-13}	7.1×10^{38}	15
FGW 6946-C	...	1.50	195	1.1×10^{-14}	3.5×10^{37}	1

Notes to Table 2.

(1) HII identification used in this work; (2) Cross-identifications: ‘MRS’ indicates those HII regions observed in the MRS study and ‘HK’ refers to the Hodge & Kennicutt atlas of HII regions (Hodge & Kennicutt 1983); (3) deprojected galactocentric distance, expressed in terms of the optical radius, R₂₅ ; (4) diameter in parsecs; (5) observed H α flux, in erg s⁻¹ cm⁻² ; (6) H α luminosity (erg s⁻¹), calculated using the distances presented in Table 1, and with no correction made for internal extinction; (7) approximate number of O5V stars enclosed, assuming ionization bounded HII regions, and the Lyc fluxes presented in Vacca et al (1996).

This figure "ferguson.fig3.jpg" is available in "jpg" format from:

<http://arxiv.org/ps/astro-ph/9805166v1>

TABLE 3. Emission Line Intensities for NGC 628

Line	FGW 628-A		FGW 628-B		FGW 628-C	
	I_{obs}	I_{cor}	I_{obs}	I_{cor}	I_{obs}	I_{cor}
[<i>OII</i>] 3727	1.305(0.031)	2.067(0.135)	3.366(0.079)	3.626(0.237)	3.287(0.082)	3.600(0.250)
H β 4861	1.000(0.033)	1.000 (0.033)	1.000(0.033)	1.000(0.033)	1.000(0.036)	1.000(0.036)
[<i>OIII</i>] 4959	0.093(0.004)	0.089(0.004)	0.563(0.019)	0.559(0.019)	0.601(0.022)	0.596(0.023)
[<i>OIII</i>] 5007	0.167(0.006)	0.156(0.006)	1.626(0.054)	1.609(0.055)	1.795(0.063)	1.772(0.064)
[<i>NII</i>] 6548	0.498(0.017)	0.282(0.023)	0.156(0.006)	0.143(0.012)	0.120(0.008)	0.107(0.011)
H α 6563	5.064(0.167)	2.851(0.235)	3.107(0.103)	2.831(0.236)	3.195(0.111)	2.852(0.251)
[<i>NII</i>] 6583	1.529(0.050)	0.857(0.071)	0.498(0.017)	0.453(0.038)	0.311(0.014)	0.277(0.026)
[<i>SII</i>] 6717	0.613(0.021)	0.332(0.029)	0.410(0.014)	0.371(0.033)	0.291(0.013)	0.258(0.025)
[<i>SII</i>] 6731	0.459(0.015)	0.248(0.022)	0.298(0.011)	0.270(0.024)	0.211(0.011)	0.187(0.019)
EW(H β) ^a	...	94.7	...	37.7	...	102.5
C(H β)	...	0.78(0.10)	...	0.13(0.10)	...	0.15(0.11)
log([<i>OII</i>]/[<i>OIII</i>])	...	0.92(0.03)	...	0.22(0.03)	...	0.18(0.03)
log(R ₂₃)	...	0.36(0.03)	...	0.76(0.02)	...	0.78(0.02)
log([<i>NII</i>]6583/[<i>OII</i>])	...	-0.38(0.05)	...	-0.90(0.05)	...	-1.11(0.05)
log([<i>OIII</i>]/[<i>NII</i>])	...	-0.67	...	0.56	...	0.79

^aEmission line equivalent width, measured in angstroms.

TABLE 3. Emission Line Intensities for NGC 628 (Continued)

Line	FGW 628-D		FGW 628-E		FGW 628-F	
	I_{obs}	I_{cor}	I_{obs}	I_{cor}	I_{obs}	I_{cor}
[<i>OII</i>] 3727	3.767(0.096)	4.042(0.292)	2.120(0.052)	2.249(0.150)	2.131(0.051)	2.207(0.147)
H β 4861	1.000(0.038)	1.000(0.038)	1.000(0.034)	1.000(0.034)	1.000(0.034)	1.000(0.034)
[<i>OIII</i>] 4959	0.643(0.026)	0.639(0.026)	1.251(0.043)	1.245(0.043)	1.369(0.046)	1.365(0.047)
[<i>OIII</i>] 5007	1.454(0.053)	1.440(0.054)	3.415(0.115)	3.387(0.118)	3.991(0.134)	3.971(0.138)
[<i>NII</i>] 6548	0.122(0.012)	0.112(0.014)	0.060(0.003)	0.056(0.005)	0.047(0.003)	0.045(0.005)
H α 6563	3.113(0.112)	2.851(0.261)	3.072(0.103)	2.853(0.241)	2.979(0.100)	2.852(0.240)
[<i>NII</i>] 6583	0.440(0.020)	0.403(0.039)	0.200(0.008)	0.186(0.016)	0.143(0.006)	0.137(0.012)
[<i>SII</i>] 6717	0.387(0.018)	0.353(0.036)	0.167(0.007)	0.155(0.014)	0.160(0.007)	0.153(0.014)
[<i>SII</i>] 6731	0.235(0.013)	0.214(0.023)	0.111(0.005)	0.103(0.010)	0.094(0.005)	0.090(0.009)
EW(H β) ^a	...	54.1	...	248.4	...	148.2
C(H β)	...	0.12(0.11)	...	0.10(0.11)	...	0.06(0.10)
log([<i>OII</i>]/[<i>OIII</i>])	...	0.29(0.03)	...	-0.32(0.03)	...	-0.38(0.03)
log(R ₂₃)	...	0.79(0.02)	...	0.84(0.02)	...	0.88(0.01)
log([<i>NII</i>]6583/[<i>OII</i>])	...	-1.00(0.05)	...	-1.08(0.05)	...	-1.21(0.05)
log([<i>OIII</i>]/[<i>NII</i>])	...	0.61	...	1.3	...	1.5

^aEmission line equivalent width, measured in angstroms.

TABLE 4. Emission Line Intensities for NGC 1058

Line	FGW 1058-A		FGW 1058-B		FGW 1058-C	
	I_{obs}	I_{cor}	I_{obs}	I_{cor}	I_{obs}	I_{cor}
[<i>OII</i>] 3727	1.368(0.037)	1.857(0.130)	1.223(0.030)	1.452(0.097)	1.272(0.037)	1.595(0.113)
H β 4861	1.000(0.038)	1.000 (0.038)	1.000(0.034)	1.000(0.034)	1.000(0.037)	1.000(0.037)
[<i>OIII</i>] 4959	0.018(0.007)	0.017(0.007)	0.060(0.005)	0.059(0.005)	0.096(0.009)	0.094(0.009)
[<i>OIII</i>] 5007	0.120(0.010)	0.115(0.010)	0.206(0.008)	0.201(0.008)	0.274(0.012)	0.265(0.012)
[<i>NII</i>] 6548	0.341(0.015)	0.233(0.021)	0.394(0.014)	0.318(0.027)	0.303(0.013)	0.229(0.021)
H α 6563	4.130(0.148)	2.820(0.249)	3.529(0.118)	2.847(0.239)	3.791(0.132)	2.856(0.251)
[<i>NII</i>] 6583	1.005(0.038)	0.684(0.061)	1.196(0.040)	0.963(0.082)	0.951(0.034)	0.714(0.064)
[<i>SII</i>] 6717	0.529(0.022)	0.352(0.034)	0.577(0.020)	0.459(0.041)	0.225(0.010)	0.166(0.016)
[<i>SII</i>] 6731	0.371(0.017)	0.247(0.024)	0.438(0.015)	0.348(0.031)	0.302(0.013)	0.223(0.022)
EW(H β) ^a	...	22.7	...	92.1	...	199.3
C(H β)	...	0.52(0.11)	...	0.29(0.10)	...	0.38(0.11)
log([<i>OII</i>]/[<i>OIII</i>])	...	1.15(0.05)	...	0.75(0.03)	...	0.65(0.04)
log(R ₂₃)	...	0.30(0.03)	...	0.23(0.03)	...	0.29(0.03)
log([<i>NII</i>]6583/[<i>OII</i>])	...	-0.43(0.05)	...	-0.18(0.05)	...	-0.35(0.05)
log([<i>OIII</i>]/[<i>NII</i>])	...	-0.84	...	-0.69	...	-0.42

^aEmission line equivalent width, measured in angstroms.

TABLE 4. Emission Line Intensities for NGC 1058 (Continued)

Line	FGW 1058-D		FGW 1058-E		FGW 1058-F	
	I_{obs}	I_{cor}	I_{obs}	I_{cor}	I_{obs}	I_{cor}
[<i>OII</i>] 3727	1.965(0.047)	2.381(0.157)	2.739(0.064)	3.025(0.196)	2.511(0.085)	2.790(0.252)
H β 4861	1.000(0.034)	1.000(0.034)	1.000(0.033)	1.000(0.033)	1.000(0.053)	1.000(0.053)
[<i>OIII</i>] 4959	0.219(0.008)	0.215(0.008)	0.786(0.026)	0.779(0.026)	0.932(0.050)	0.923(0.049)
[<i>OIII</i>] 5007	0.512(0.018)	0.499(0.018)	2.298(0.076)	2.267(0.077)	2.735(0.126)	2.695(0.128)
[<i>NII</i>] 6548	0.336(0.012)	0.265(0.022)	0.135(0.005)	0.119(0.010)	0.153(0.024)	0.134(0.025)
H α 6563	3.616(0.120)	2.844(0.237)	3.231(0.106)	2.854(0.235)	3.534(0.162)	3.100(0.0354)
[<i>NII</i>] 6583	1.037(0.035)	0.814(0.068)	0.414(0.014)	0.365(0.030)	0.386(0.035)	0.338(0.047)
[<i>SII</i>] 6717	0.502(0.017)	0.388(0.034)	0.362(0.012)	0.317(0.028)	0.371(0.042)	0.322(0.051)
[<i>SII</i>] 6731	0.382(0.013)	0.295(0.026)	0.257(0.009)	0.225(0.020)
EW(H β) ^a	...	50.5	...	228.6	...	55.1
C(H β)	...	0.33(0.10)	...	0.17(0.10)	...	0.18(0.14)
log([<i>OII</i>]/[<i>OIII</i>])	...	0.52(0.03)	...	0.00(0.03)	...	-0.11(0.04)
log(R ₂₃)	...	0.49(0.03)	...	0.78(0.02)	...	0.81(0.02)
log([<i>NII</i>]6583/[<i>OII</i>])	...	-0.47(0.05)	...	-0.92(0.05)	...	-0.92(0.07)
log([<i>OIII</i>]/[<i>NII</i>])	...	-0.18	...	0.80	...	0.88

^aEmission line equivalent width, measured in angstroms.

TABLE 4. Emission Line Intensities for NGC 1058 (Continued)

Line	FGW 1058-G		FGW 1058-H	
	I_{obs}	I_{cor}	I_{obs}	I_{cor}
[<i>OII</i>] 3727	4.133(0.101)	4.251(0.297)	1.950(0.052)	2.019(0.142)
H β 4861	1.000(0.037)	1.000(0.037)	1.000(0.037)	1.000(0.037)
[<i>OIII</i>] 4959	0.137(0.009)	0.137(0.009)	1.148(0.042)	1.144(0.043)
[<i>OIII</i>] 5007	0.458(0.018)	0.456(0.019)	3.282(0.117)	3.266(0.120)
[<i>NII</i>] 6548	0.114(0.010)	0.110(0.013)	0.099(0.009)	0.095(0.011)
H α 6563	2.943(0.103)	2.842(0.252)	2.980(0.106)	2.853(0.254)
[<i>NII</i>] 6583	0.321(0.015)	0.310(0.029)	0.179(0.009)	0.171(0.017)
[<i>SII</i>] 6717	0.578(0.022)	0.557(0.053)	0.238(0.011)	0.228(0.023)
[<i>SII</i>] 6731	0.424(0.017)	0.410(0.040)	0.148(0.008)	0.141(0.015)
EW(H β) ^a	...	62.2	...	130.5
C(H β)	...	0.05(0.11)	...	0.06(0.11)
log([<i>OII</i>]/[<i>OIII</i>])	...	0.86(0.03)	...	-0.34(0.03)
log(R ₂₃)	...	0.68(0.03)	...	0.81(0.02)
log([<i>NII</i>]6583/[<i>OII</i>])	...	-1.14(0.05)	...	-1.04(0.05)
log([<i>OIII</i>]/[<i>NII</i>])	...	0.14	...	1.22

^aEmission line equivalent width, measured in angstroms.

TABLE 5. Emission Line Intensities for NGC 6946

Line	FGW 6946-A		FGW 6946-B		FGW 6946-C	
	I_{obs}	I_{cor}	I_{obs}	I_{cor}	I_{obs}	I_{cor}
[OII] 3727	1.669(0.039)	2.458(0.159)	1.411(0.039)	2.111(0.146)	2.978(0.078)	3.792(0.270)
H β 4861	1.000(0.033)	1.000(0.033)	1.000(0.036)	1.000(0.036)	1.000(0.038)	1.000(0.038)
[OIII] 4959	0.586(0.019)	0.565(0.019)	0.123(0.008)	0.119(0.008)	0.156(0.010)	0.153(0.010)
[OIII] 5007	1.764(0.058)	1.672(0.057)	0.383(0.016)	0.362(0.015)	0.698(0.027)	0.675(0.027)
[NII] 6548	0.350(0.012)	0.217(0.018)	0.427(0.017)	0.259(0.023)	0.105(0.009)	0.078(0.009)
H α 6563	4.621(0.151)	2.850(0.235)	4.709(0.163)	2.846(0.246)	3.857(0.139)	2.853(0.257)
[NII] 6583	1.083(0.036)	0.665(0.055)	1.394(0.049)	0.838(0.073)	0.308(0.015)	0.227(0.022)
[SII] 6717	0.631(0.021)	0.377(0.033)	0.672(0.025)	0.393(0.036)	0.333(0.016)	0.242(0.024)
[SII] 6731	0.481(0.016)	0.286(0.025)	0.436(0.017)	0.254(0.024)	0.204(0.012)	0.148(0.016)
EW(H β) ^a	...	120.2	...	146.8	...	100.3
C(H β)	...	0.66(0.10)	...	0.68(0.11)	...	0.41(0.11)
log([OII]/[OIII])	...	0.04(0.03)	...	0.64(0.03)	...	0.66(0.03)
log(R ₂₃)	...	0.67(0.02)	...	0.41(0.02)	...	0.66(0.03)
log([NII]6583/[OII])	...	-0.57(0.05)	...	-0.40(0.05)	...	-1.22(0.05)
log([OIII]/[NII])	...	0.40	...	-0.36	...	0.43

^aEmission line equivalent width, measured in angstroms.

TABLE 6. Derived Oxygen and Nitrogen Abundances

HII ID	R/R ₂₅	A _V	O/H	N/O	<U>	[SII]6717/[SII]6731
FGW 628-A	0.25	1.66	-3.08(u)	-0.98	2.2×10^{-4}	1.34
FGW 628-B	0.74	0.27	-3.40(u)	-1.23	1.2×10^{-3}	1.38
FGW 628-C	1.14	0.33	-3.92(l)	-1.41	9.3×10^{-4}	1.38
FGW 628-D	1.14	0.25	-3.87(l)	-1.32	7.3×10^{-4}	1.65
FGW 628-E	1.30	0.21	-3.98(l)	-1.36	3.1×10^{-4}	1.50
FGW 628-F	1.73	0.13	-3.93(l)	-1.45	3.7×10^{-3}	1.71
FGW 1058-A	0.20	1.11	-3.04(u)	-1.07	1.2×10^{-4}	1.43
FGW 1058-B	0.26	0.62	-3.01(u)	-0.85	3.9×10^{-4}	1.32
FGW 1058-C	0.41	0.82	-3.03(u)	-0.99	5.0×10^{-4}	0.75
FGW 1058-D	0.60	0.70	-3.15(u)	-0.99	6.3×10^{-4}	1.32
FGW 1058-E	1.03	0.36	-3.40(u)	-1.23	2.2×10^{-3}	1.41
FGW 1058-F	1.28	0.38	-3.41(u)	-1.19	2.9×10^{-3}	...
FGW 1058-G	1.88	0.10	-3.82(l)	-1.51	1.7×10^{-4}	1.36
FGW 1058-H	1.93	0.13	-4.05(l)	-1.29	3.2×10^{-3}	1.62
FGW 6946-A	0.61	1.40	-3.28(u)	-0.96	2.1×10^{-3}	1.32
FGW 6946-B	0.65	1.46	-3.10(u)	-0.98	4.7×10^{-4}	1.55
FGW 6946-C	1.50	0.87	-3.93(l)	-1.61	2.8×10^{-4}	1.63

Notes to Table 6.

The letter which follows the O/H abundance indicates whether the upper (u) or lower (l) branch of the log (O/H)–log R₂₃ was assumed in the calculation. The probable errors on the quantities presented here are discussed in the text.

TABLE 7. Derived Radial Abundance Gradients

Galaxy	$\log(\text{O}/\text{H})$ at $R=0$	$\log(\text{O}/\text{H})$ [dex/ R_{25}]	$\log(\text{O}/\text{H})$ [dex/kpc]	$\log(\text{N}/\text{O})$ at $R=0$	$\log(\text{N}/\text{O})$ [dex/ R_{25}]	$\log(\text{N}/\text{O})$ [dex/kpc]	A_V [dex/ R_{25}]
NGC 628	-2.92	-0.73 ± 0.12	-0.05 ± 0.01	-0.90	-0.37 ± 0.06	-0.02 ± 0.01	-1.07
NGC 1058	-2.85	-0.55 ± 0.11	-0.13 ± 0.01	-0.89	-0.26 ± 0.06	-0.06 ± 0.01	-0.46
NGC 6946	-2.77	-0.70 ± 0.19	-0.08 ± 0.01	-0.59	-0.63 ± 0.10	-0.07 ± 0.01	-0.70